Polydopamine Nanoparticle-Based Combined Chemotherapy and Photothermal Therapy for the Treatment of Liver Cancer

(Article begins on next page)

05 February 2025

Polydopamine Nanoparticle-Based Combined Chemotherapy and Photothermal Therapy for the Treatment of Liver Cancer

Melis Emanet,* Marie Celine Lefevre, Maria Cristina Ceccarelli, Matteo Battaglini, Alessio Carmignani, Francesco Schiavone, Attilio Marino, Daniele De Pasquale, Mirko Prato, Francesco De Boni, Andrea Petretto, Martina Bartolucci, Federico Catalano, Stefania Moscato, and Gianni Ciofani*

Read Online

ACCESS | Metrics & More | Article Recommendations | SI Supporting Information

ABSTRACT: Polydopamine nanoparticles (PDA NPs) are proposed as an anti-cancer tool against hepatocellular carcinoma through the combination of near-infrared (NIR)-mediated hyperthermia and loading with a chemotherapeutic drug, sorafenib (SRF). Cell membranes isolated from a liver cancer cell line (HepG2) have been exploited for the coating of the nanoparticles (thus obtaining CM−SRF−PDA NPs), to promote homotypic targeting toward cancer cells. The selective targeting ability and the combined photothermal and chemotherapeutic activity of the CM−SRF−PDA NPs following NIR irradiation have been evaluated on cell cultures in static and dynamic conditions, besides three-dimensional culture models. Eventually, the therapeutic effectiveness of the proposed approach has also been tested *ex ovo* on HepG2 spheroid-grafted quail embryos. This comprehensive investigation, supported by proteomic analysis, showed the effectiveness of the proposed nanoplatform and strongly suggests further pre-clinical testing in the treatment of liver cancer.

KEYWORDS: polydopamine nanoparticles, homotypic targeting, sorafenib, photothermal therapy, liver cancer
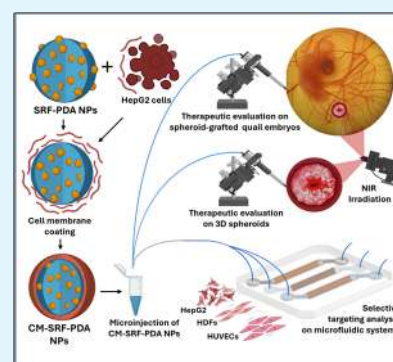
1. INTRODUCTION

Hepatocellular carcinoma (HCC) is the fifth most common neoplasia worldwide and represents the third leading cause of cancer-related death globally. The risk factors that increase the incidence of HCC are hepatitis B and hepatitis C virus infections, aflatoxin exposure, high alcohol consumption, and smoking.[1] The 5-year survival after diagnosis, strictly related to the stage of the disease, has been estimated between 48 and 75%.[2] The therapeutic strategies may change based on the liver conditions and the tumor stage:[3] surgical resection, liver transplantation, and local ablation can improve the survival of HCC patients at an early-stage diagnosis, but no effective treatments are available for patients with advanced HCC.[4]

In recent years, however, promising advances achieved in the knowledge of molecular mechanisms underlying the growth of HCC allowed for the development of new approaches useful for the treatment of hypervascularized HCC tumors. *In vivo* and *in vitro* studies have demonstrated that sorafenib (SRF), a multi-kinase inhibitor, is able to block tumor growth by inhibiting important pathways involved in protein biosynthesis, cell proliferation, and angiogenesis of the tumor, by acting on serine−threonine kinases (Raf-1 and B-Raf), the tyrosine kinase activity of vascular endothelial growth factor receptors (VEGFR-2 and VEGRF-3), and platelet-derived growth factor receptor β (PDGFR-β).[5]

Some issues are, however, related to the use of SRF. Especially in the case of long-term therapies, this drug can generate hypoxia in HCC cells, a situation that stimulates drug resistance-based cell survival by activating homeostasis mechanisms. Moreover, its poor solubility in aqueous environments strongly limits its widespread application.[6] All of this considered, a SRF delivery system together with a complementary therapeutic strategy may be a suitable approach to develop an efficient treatment against HCC, by also avoiding significant side effects occurring as a result of an untargeted administration of the drug in the whole organism.[7]

Nanomedicine is paving the way to develop new nano-objects and "smart" materials capable of increasing the localization of therapeutic and diagnostic agents, enhancing therapeutic efficacy and tolerance to therapy by minimizing the side effects.[8] As far as SRF is concerned, a limited number of examples of delivery systems can be found in the literature, including dual polymeric lipid nanoparticles,[9] poly(lactic-*co*-glycolic) acid (PLGA) microspheres,[10] solid lipid nanoparticles,[11] or porous silicon nanoparticles.[12] "Smart" (i.e., stimuli-responsive) nanoparticles, besides acting as drug vectors, can also be exploited as

nanotransducers to provide complementary "physical" therapies. For example, nanostructures like gold nanoparticles (AuNPs) and gold nanorods (AuNRs) have been widely investigated as photothermal therapeutic agents, in particular, for cancer therapy.[13] A drawback of such approaches, however, relies on the inorganic nature of the nanovectors: the lack of substantial biodegradability is a concern of systemic toxicity in long-term applications, jointly to accumulation in the reticuloendothelial system and in other excretory organs.[14] Considering their highly biocompatible and biodegradable nature and the ability to convert near-infrared light into heat, polydopamine nanoparticles (PDA NPs) have gained significant interest as photothermal therapy agents. Additionally, the relatively high drug loading capacity of these nanostructures (depending upon the chemical/physical features of the encapsulated substance) make them ideal candidates as drug delivery systems, thus providing an efficient tool for combined multiple therapeutic approaches.[15]

With regard to the targeted delivery, homotypic recognition by cancer cells is a biomimetic approach actively exploited over the last few decades. This recognition is mediated by specific membrane proteins of cancer cells that are involved in cell–cell interaction and adhesiveness.[16] Homotypic targeting is achieved by coating nanomaterials with cancer cell membranes, thus allowing recognition and promotion of the uptake by cancer cells themselves. Besides being an efficient targeting approach, this strategy also avoids immune reactions and improves the stability of the NPs in biological environments.[17] Some relevant examples are also given by previous works from our group, including the first example of smart nanoparticles coating with patient-derived cancer cells.[18]

In this work, PDA NPs have been proposed for a combined therapeutic approach against liver cancer following homotypic targeting, through the delivery of the chemotherapy drug SRF and near-infrared (NIR)-mediated photothermal therapy. After an extensive physical/chemical characterization of the nanovectors, biocompatibility, targeting efficiency, and combined therapeutic effects have been evaluated on dynamic cell cultures, three-dimensional (3D) HepG2-derived spheroids, and eventually *ex ovo* on a HepG2 spheroid-grafted chorioallantoic membrane model of quail embryos. An in-depth proteomic analysis completed the work, suggesting extremely promising clinical perspectives of the proposed approach.

2. MATERIALS AND METHODS

2.1. Preparation of SRF–PDA NPs. SRF–PDA NPs have been synthesized by following a classic Stöber reaction, with some modifications.[19] Briefly, SRF (2 mg) was dissolved in 200 μL of dimethyl sulfoxide (DMSO), then mixed with a dopamine solution (25 mg, dissolved in 1 mL of Milli-Q water), and then added to a solution including Milli-Q water (4.5 mL), ethanol (2 mL), and ammonium hydroxide (NH$_4$OH, 150 μL) while stirring at a constant speed (600 rpm) at 30 °C. Following overnight stirring, the obtained SRF–PDA NP suspension was washed in Milli-Q water by centrifugation at 15000g (Sorvall LYNX 4000 Superspeed Centrifuge, Thermo Fisher) for 15 min at 4 °C. The washing step was repeated 3 times, and eventually SRF–PDA NPs were re-suspended in Milli-Q water and stored at 4 °C for further experiments. For the assessment of the production yield, an aliquot of sample (100 μL) was freeze-dried and the obtained mass was weighed. To obtain fluorescent-stained nanoparticles, rhodamine 123 (0.4 mg) was added during the synthesis process.

2.2. Cell Cultures. Human hepatocellular carcinoma cells (HepG2) were purchased from American Type Culture Collection (ATCC, HB-8065) and cultured in minimum essential medium (MEM, EuroClone) supplemented with 10% heat-inactivated fetal bovine serum (FBS), 1%

sodium pyruvate (1 mM), and 1% penicillin–streptomycin (100 units/mL penicillin and 100 μg/mL streptomycin).

Human dermal fibroblasts (HDFs) have been purchased from ATCC (PCS-201-012) and cultured in high-glucose Dulbecco's modified Eagle's medium (DMEM, EuroClone) supplemented with 10% heat-inactivated FBS, 1% sodium pyruvate (1 mM), and 1% penicillin–streptomycin (100 units/mL penicillin and 100 μg/mL streptomycin).

Human umbilical vein endothelial cells (HUVECs), a kind gift from Dr. Serena del Turco [Consiglio Nazionale delle Ricerche (CNR), Italy], were cultured in EndoGRO basal medium (SCME-BM, Millipore) added with the EndoGRO-VEGF supplemented kit (SCME002-S, Millipore).

All of the cell cultures were maintained at 37 °C in a 5% CO$_2$ humidified atmosphere. The experiments were performed on cells within 10–20 passages.

2.3. Cell Membrane Coating. Cell membrane isolation has been performed by following a protocol developed in our group, with minor modifications.[20] HepG2 cells were seeded in Petri dishes (150 mm in diameter, Corning) at a density of 2×10^4 cells/cm^2 and detached with a scraper when 90% confluency was reached. After three washing steps in phosphate-buffered saline (PBS) by centrifugation at 700g for 5 min at 24 °C, 5×10^6 HepG2 cells were resuspended in 1 mL of de-ionized water and disrupted with a high-pressure homogenizer (20 psi). A purification cycle was performed with a centrifuge step at 10000g for 10 min. Eventually, the supernatant, potentially containing cell membranes, was collected and centrifuged at 37000g for 60 min. The obtained pellet was finally re-suspended in 1 mL of de-ionized water for further processing.

For nanoparticle dispersion, 1 mL of SRF–PDA NPs (1 mg/mL) was sonicated with an ultrasonic probe (Fisherbrand Q125 sonicator) for 10 min at 50% amplitude in an ice bath; thereafter, 1 mL of CM extract (derived from 5×10^6 HepG2 cells) was added to the dispersion and sonicated for 20 min, applying the same parameters. CM-coated SRF–PDA NPs (CM–SRF–PDA NPs) were washed 3 times by centrifugation at 15000g for 15 min at 4 °C with de-ionized water. For further investigations, CM–SRF–PDA NPs were re-suspended in 1 mL of de-ionized water to have a final concentration of 1 mg/mL.

For fluorescence tracking, CM-coated nanoparticles (1 mg/mL) were stained with the DiI dye (0.2 μg, Invitrogen) by stirring the dispersion for 4 h at room temperature; a washing step in Milli-Q water by centrifugation at 15000g for 15 min at 4 °C followed.

2.4. Characterization of CM–SRF–PDA NPs. Raman spectroscopy was carried out to verify the formation of polydopamine from the dopamine monomer. The samples (1 mg/mL PDA NPs and, as a control, 1 mg/mL dopamine hydrochloride) dispersed in Milli-Q water were dropped on Raman-grade calcium fluoride substrates (Crystran), and a Horiba LabRAM HR evolution confocal Raman microscope, equipped with a 532 nm laser and a 10× objective, was used to acquire the signals at 3.2% laser power. Each sample spectrum was obtained from 16 scans (3 s acquisition time and 10 accumulations) in the wavenumber range of 300–3500 cm^{-1}. Spectra were acquired from three different locations per sample, and appropriate baseline correction has been performed.

The morphological analysis of the nanovectors was performed with scanning electron microscopy (SEM) and transmission electron microscopy (TEM). For the SEM imaging, the samples (2 μL, 100 μg/mL) were placed on a silicon substrate and left to dry for 2 h at room temperature. Then, the samples were gold-sputtered using a Quorum Tech Q150RES gold sputter coater (30 mA for 30 s), and their images were acquired using a dual-beam SEM system, Helios NanoLab 600i FIB/SEM, FEI. The TEM images of the samples were acquired using a JEOL JEM1011 transmission electron microscope equipped with a thermionic electron source (tungsten) and operating at 100 kV. A drop of the sample dispersion was placed on a Cu grid, coated with an ultrathin amorphous carbon film, previously plasma treated (O$_2$ + Ar plasma, 10 W, 2 min) to remove hydrocarbon residues from carbon film deposition. To enhance the contrast of the lipid coating of the particles, the procedure included a 60 s negative staining using uranyl acetate solution (1%, v/v).

The colloidal stability has been evaluated by measuring the hydrodynamic size distribution and the polydispersity index (PDI) of SRF−PDA and CM−SRF−PDA NPs in Milli-Q water, PBS, and complete cellular medium, in addition to the ζ-potential Milli-Q water, using a ZetaSizer (Malvern Instruments). The samples were dispersed at 50 μg/mL in 1 mL of solution, and three measurements at room temperature were performed.

The photothermal response of the samples was evaluated by measuring the temperature change before and after NIR light irradiation. An aqueous dispersion of CM−SRF−PDA NPs (100 μg/mL) was prepared in a Willco dish, and the initial temperature was kept constant at 37 °C by placing it in a water bath. Then, the sample was exposed to the NIR light (RLTMDL-808-500 NIR laser, with λ of 808 nm, spot diameter of 2.5 mm, and laser power of 1.54 W/cm²) for 10 min; meanwhile, the temperature of the dispersion was constantly measured by a FLIR thermal camera (A300).

SRF−PDA NPs and CM−SRF−PDA NPs have been analyzed by high-resolution X-ray photoelectron spectroscopy (XPS) to identify the present elements and their electronic states. The XPS measurements were carried out through a Kratos Axis Ultra^{DLD} spectrometer (Kratos Analytical, Ltd.) with a monochromated Al Kα X-ray source (hν = 1486.6 eV) operating at 20 mA and 15 kV. Both samples were prepared by drop casting a few microliters of an aqueous suspension on a freshly cleaved graphite substrate. The wide scans were collected over an analysis area of 300×700 μm² at a photoelectron pass energy of 160 eV and with energy steps of 1 eV, while high-resolution spectra were collected at a photoelectron pass energy of 20 eV and energy steps of 0.1 eV. Differential electrical charging effects on the surface of the sample were neutralized during the measurements. Obtained spectra were analyzed with CasaXPS software (Casa Software, Ltd., version 2.3.24), and the residual background was eliminated by the Shirley method.

For the evaluation of the encapsulation efficiency (EE) and loading capacity (LC) of CM−SRF−PDA NPs, the drug loaded in the nanoparticles (W_{loaded}) has been assessed by dissolving freeze-dried samples of known weight ($W_{freeze-dried}$) in a DMSO/water (1:1, v/v) solution, and keeping them at 80 °C for 2 h under stirring. Thereafter, samples were centrifuged at 15000g for 15 min at 4 °C. The supernatants were analyzed using a HPLC Shimadzu LC-20A for SRF detection. The mobile phase was a mixture of acetic acid and water (75:25, v/v) at a flow rate of 1 mL/min. The injection volume and ultraviolet (UV) wavelength were set as 5 mL and 365 nm, respectively. Standard samples of SRF in DMSO/water solution have been previously prepared and analyzed to obtain a calibration curve. The EE and LC of SRF−PDA NPs were calculated using eqs 1 and 2, respectively, where W_{total} represents the total amount drug at the beginning of the preparation procedure.

$$EE\ (\%) = \frac{W_{loaded}}{W_{total}} \times 100 \tag{1}$$

$$LC\ (\%) = \frac{W_{loaded}}{W_{freeze-dried}} \times 100 \tag{2}$$

SRF cumulative release investigation has been performed in PBS at different time points (1, 4, 24, and 72 h) and different pH values (pH 4.5 and 7.4) in either the presence or absence of NIR stimulation (10 min/day for 3 days, at 0.541 W/cm²), through high-performance liquid chromatography (HPLC) analysis as previously described.

2.5. Cell Metabolic Activity and Proliferation Assays. The metabolic activity of HepG2 cells following treatment with nanovectors and controls was evaluated with a WST-1 colorimetric assay (BioVision). Cells were seeded in a 96 well plate (Sarstedt) at a density of 1.8×10^4 cells/cm² and incubated for 24 h. Then, the cultures were treated with increasing concentrations (0−500 μg/mL) of PDA NPs, SRF−PDA NPs, CM−SRF−PDA NPs, and SRF (the latter at 0−1.15 μg/mL, corresponding to the concentrations loaded in 0−500 μg/mL NPs) and further incubated for 24 and 72 h. Thereafter, the cell culture medium was replaced with WST-1 reagent (Abcam) diluted in MEM without phenol red (1:10, Gibco). Following a 40 min incubation at 37 °C, the supernatants were collected and their absorbance at 440

nm was assessed with a VictorX3 plate reader (Perkin Elmer). Experiments were performed in triplicate.

Cell proliferation was evaluated following the same treatments using the Quant-iT PicoGreen dsDNA assay kit, following the instructions of the manufacturer. In this assay, the cells were washed 3 times with PBS and then left in 100 μL of de-ionized water. Subsequently, the samples underwent 3 cycles of freezing (at −80 °C) and thawing (at 37 °C) to allow for complete cell lysis. To evaluate the dsDNA content, 100 μL of reaction buffer, 50 μL of cell lysate, and 150 μL of PicoGreen reagent were mixed in black polystyrene plates (Corning Costar). Following the incubation for 10 min at room temperature, fluorescence emission (directly proportional to the dsDNA content and, thus, the cell number) was measured using the VictorX3 microplate reader ($λ_{ex}$ = 485 nm and $λ_{em}$ = 535 nm); experiments were performed in triplicate.

The metabolic activity and proliferation of HepG2 cells were also assessed after SRF (0.23 μg/mL, corresponding to 100 μg/mL CM−SRF−PDA NPs), CM−PDA NPs (100 μg/mL), and CM−SRF−PDA NPs (100 μg/mL) treatment in the absence or presence of NIR stimulation, to evaluate the therapeutic efficacy of the proposed approach. The assays have been carried out just as described; the NIR light (808 nm) was applied 10 min/day for 3 days at 0.541 W/cm². Then, the WST-1 and PicoGreen assays were performed by following the same above-described protocols.

2.6. Cellular Internalization in Static Conditions. For confocal imaging, HepG2 cells were seeded at 2×10^4 cells/cm² in μ-Dishes (35 mm, Ibidi) and incubated for 24 h; thereafter, they were treated with either PDA NPs or CM−PDA NPs (100 μg/mL) and incubated for a further 24 h. Following 3 washing steps with PBS (Sigma-Aldrich), the cells were fixed with 4% paraformaldehyde (PFA, Sigma-Aldrich) at 4 °C for 30 min and rinsed again with PBS 3 times. The cells were treated with Hoechst 33342 (1:1000, v/v, Invitrogen, with $λ_{ex}$ = 350 nm and $λ_{em}$ = 461 nm) and TRITC−phalloidin (1:200, v/v, Sigma-Aldrich, with $λ_{ex}$ = 495 nm and $λ_{em}$ = 513 nm) at 37 °C for 45 min for the staining of nuclei and f-actin, respectively. The samples were imaged with confocal microscopy (C2 system, Nikon); a far-red laser ($λ_{ex}$ = 720 nm) was exploited for label-free imaging of the nanoparticles.

Internalization was further investigated, quantitatively, through flow cytometry by exploiting rhodamine-labeled nanoparticles by following the same protocol described for confocal imaging. At the end of the treatment, the cells were collected through 3 centrifugation steps at 700g for 5 min at 24 °C. The pellets were finally re-suspended in PBS and analyzed by flow cytometry (Beckman Coulter CytoFLEX, with $λ_{ex}$ = 488 nm and $λ_{em}$ = 530 nm).

The cellular internalization pathway and intracellular localization of the nanoparticles have also been investigated with TEM imaging. At this aim, cells were seeded in T75 flasks and incubated for 24 h; thereafter, the cultures were treated with either PDA or CM−PDA NPs for 6 and 12 h. At the end points, the cells were washed 3 times and treated with 1.5% glutaraldehyde (in PBS) for 45 min, by shaking at room temperature. The cell suspensions were then centrifuged at 670g for 10 min at 24 °C and collected as pellets; the latter was then treated with 1.5% glutaraldehyde (dissolved in 0.1 M cacodylate buffer at pH 7.4, Sigma-Aldrich) for 1 h by shaking at room temperature and eventually washed 3 times in the washing solution (0.1 M cacodylate buffer at pH 7.4) by stirring for 10 min. For post-fixation, the pellets were treated with 1% osmium tetroxide in the same buffer, washed 6 times for 10 min each, and then stained with 1% uranyl acetate in Milli-Q water overnight at 4 °C; extensive washing in Milli-Q water followed. The samples were then dehydrated with EtOH solutions at increasing concentrations and incubated with propylene oxide (PO) 3 times for 20 min. Thereafter, an overnight incubation in a mixture of PO and Epon resin was performed, followed by an incubation in pure Epon for 2 h; the samples were finally embedded by polymerizing Epon at 65 °C for 48 h. Ultrathin sections of 70 nm were cut using a Leica Ultracut EM UC 6 cryo-ultramicrotome, and TEM images were acquired with a JEOL JEM 1011 electron microscope and recorded with a 2 MP charge-coupled device camera (Orius Gatan).

2.7. Selective Targeting in Dynamic Conditions. A microfluidic system has been designed and fabricated in our laboratory for testing the targeting abilities of the nanoparticles in dynamic conditions

(Figure S1 of the Supporting Information): it has been designed with AUTO-CAD software (Autodesk) and printed on a polyester photomask from SELBA. The fabrication process involved microreplica molding (REM) by photolithography, providing a master for the implementation of soft lithography. The master was obtained on a 3 in. diameter silicon wafer previously dehydrated at 200 °C for 5 min and activated in the plasma oxygen chamber. A layer of 100 μm of SU8-50 photoresist (MicroChem, Kayaku Advance Materials) was spin-coated. Then, the photoresist was soft-baked for 10 min at 65 °C and 30 min at 95 °C and exposed to the UV light using a mask aligner (MA/BA6, SUSS MicroTec) to transfer the design to the photoresist. The silicon wafer was post-baked for 1 min at 65 °C and 10 min at 95 °C, developed with the MicroChem SU-8 developer for 10 min, and then hard-baked for 20 min at 200 °C. The thus-obtained master was used to perform the replica molding with soft lithography. The microfluidic system was manufactured with poly(dimethylsiloxane) elastomer (SYLGARD 184) mixing at a 10:1 ratio the silicone elastomer and the cross-linking agent. Then, the mixture was cast on the master, degassed, and cured for 2 h at 70 °C. Polydimethylsiloxane (PDMS) was peeled off from the master, cut, and micro-milled with a 3 mm puncher to obtain the inlets and outlets of the channels. The device was irreversibly bonded with a glass coverslip through oxygen plasma at 40 W for 15 s and baked for 20 min at 70 °C. The final microfluidic system consists of three parallel and equal rectangular channels with a height of 100 μm, a width of 2 mm, and a length of 15 mm.

A computational fluid dynamics (CFD) simulation was performed by COMSOL Multiphysics to extract information about flow and shear stress experienced by cells during the targeting experiments (Figure S2A of the Supporting Information). The culture cell medium, doped with nanoparticles, was approximated to an aqueous fluid at room temperature. The effects of stress-dependent viscosity on the flow at low Reynolds numbers can be neglected, and the fluid was considered as a Newtonian incompressible. The fluid dynamics is governed by the Navier–Stokes equations (eq 3):

$$\begin{cases} \rho(\mathbf{u}\cdot\nabla)\mathbf{u} = -\nabla P + \mu\nabla\cdot((\nabla\mathbf{u}) + (\nabla\mathbf{u})^T) & \text{on } \mathscr{B} \\ \nabla\cdot(\rho\mathbf{u}) = 0 & \text{on } \mathscr{B} \\ \mathbf{u} = [0, \mathbf{u}_y, 0] & \text{on } \partial\mathscr{B}_{\text{in}} \\ P = 0 & \text{on } \partial\mathscr{B}_{\text{out}} \\ \mathbf{u}\cdot\mathbf{n} = 0 & \text{on } \partial\mathscr{B}_{\text{wall}} \end{cases} \quad (3)$$

where $\rho \in \mathbb{R}$ (kg/m^3) is the density of the fluid (considered as high-glucose DMEM + 10% FBS; 1.006 g/cm^3 [21]), $\mathbf{u} \in \mathbb{R}^3$ (m/s) is the velocity field (with $u_y = 2.083 \times 10^{-4}$ m/s), $P \in \mathbb{R}$ (Pa) is the pressure, $\mathbf{n} \in \mathbb{R}^3$ is the normal vector to the surface $\partial\mathscr{B}_{\text{wall}}$.

The inlet condition on the velocity was calculated considering the section of the channel and a flow rate of 2.5 μL/min (4.1667 × 10^{-11} m^3/s).

Under the assumption of laminar and steady-state flow (Figure S2B of the Supporting Information), we evaluated the spatial velocity distribution along the Z component (Figure S2C of the Supporting Information) and the distribution on the XY plane of the shear stress on the bottom wall of the channel, where the cells are seeded (Figure S2D of the Supporting Information). We also extracted the XY plane streamline of the flow along the channel. The spatial distribution of the velocity has the typical parabolic profile of laminar flow, while the shear stress distribution is in accordance with the *in vivo* shear stress experienced by the cell lines used in our model, with an average value in the middle of the channel of 0.11 dyn/cm^2.[22]

Concerning selective targeting assessment, three different cell lines (HUVECs, HDFs, and HepG2 cells) were seeded in three independent channels of the microfluidic system at a density of 70 000, 70 000, and 170 000 cell/cm^2, respectively, and incubated in sterile conditions at 37 °C and 5% CO$_2$ for 24 h. Thereafter, PDA NPs or CM–PDA NPs (200 μg/mL, diluted in high-glucose DMEM) were perfused in the channels for 1 h at a flow rate of 2.5 μL/min using a microfluidic syringe pump (NE-1002X; Figure S2E of the Supporting Information). After

perfusion, the medium containing the nanoparticles was removed and the cells were washed 3 times with PBS. For confocal imaging, the cells were fixed with 4% PFA at 4 °C for 30 min and rinsed with PBS 3 times. Thereafter, the cells were stained with TRITC–phalloidin and Hoechst 33342 and monitored with confocal laser scanning microscopy, as previously described. The internalization extent was analyzed with the ImageJ software, by considering the ratio of the NP-positive cells to nucleus-stained cells.

2.8. Intracellular Temperature Analysis. For the evaluation of the photothermal conversion capacity of intracellular CM–PDA NPs and CM–SRF–PDA NPs, thermosensitive DiI dye-stained nanovectors (DiI–CM–PDA or DiI–CM–SRF–PDA NPs) were used. HepG2 cells (at the density of 1.8×10^4 cells/cm^2) were seeded in black 24-well μ-plate (with flat and clear bottoms, Ibidi) and incubated for 24 h; thereafter, the cells were treated with DiI–CM–PDA NPs or DiI–CM–SRF–PDA NPs (100 μg/mL) and incubated for a further 24 h. Time-lapse fluorescence imaging was performed using a Nikon C2+ confocal microscope equipped with a 60× oil objective and taking advantage of the automated focal control through the Nikon Perfect Focus System. Fluorescence intensities ($\lambda_{\text{ex}} = 561$ nm and $\lambda_{\text{em}} = 570$ nm) were recorded every 10 s before and during NIR exposure. Finally, fluorescence intensities were converted to temperature levels following a calibration (−2.24% fluorescence intensity/°C) as reported in a previous work of our group.[23]

2.9. Investigation of the Therapeutic Effect on Two-Dimensional (2D) Cell Cultures. Apoptotic/necrotic phenomena have been investigated in HepG2 cultures. Cells were seeded at a density of 1.8×10^4 cells/cm^2 in 96-well plates and incubated for 24 h; thereafter, the cultures were treated with SRF (0.23 μg/mL, corresponding to the content loaded in 100 μg/mL CM–SRF–PDA NPs), CM–PDA NPs (100 μg/mL), and CM–SRF–PDA NPs (100 μg/mL) for 24 h. Cultures were then exposed to NIR light stimulation for 3 days (10 min/day, 0.541 W/cm^2); non-stimulated and non-treated cultures were considered as well as controls. Following the stimulation, the cells were stained with annexin V–fluorescein isothiocyanate (FITC) (0.4 μg/mL in PBS) and propidium iodide (PI, 0.1 μg/mL in PBS) and incubated for 15 min in the dark at room temperature. Flow cytometry analysis followed (annexin V–FITC, $\lambda_{\text{ex}} = 485$ nm and $\lambda_{\text{em}} = 535$ nm; PI, $\lambda_{\text{ex}} = 535$ nm and $\lambda_{\text{em}} = 615$ nm), to determine the percentages of healthy, necrotic, apoptotic, and late apoptotic cells in all of the experimental classes; three independent experiments were performed.

For cell cycle analysis, cultures (the same experimental classes previously introduced) were fixed with ethanol (70%) at −20 °C for 24 h. Thereafter, for the removal of ethanol, they were centrifuged at 670g for 5 min and washed in bovine serum albumin (BSA) solution (0.5%, w/v, in PBS) 3 times. Then, the cells were treated with a RNase solution (50 μg/mL) for 20 min and underwent further centrifugation (at 670g for 5 min). In the final step, the cells were stained with PI (0.1 μg/mL in PBS) and incubated for 15 min in the dark at room temperature. The cells were eventually analyzed by flow cytometry as previously described, and the percentages of cells in the G1, S, and G2/M phases were calculated from collected fluorescence data; three independent experiments were performed.

The therapeutic effect of the nanostructures has been also evaluated on HepG2 cells in terms of specific protein expression, namely, Ki-67, p53, and HSP70, on the same experimental classes. At this aim, cells were seeded in black 24-well μ-plates (with flat and clear bottoms, Ibidi); at the end of the treatment protocols, cells were fixed with PFA (4%, w/v, in PBS), incubated at 4 °C for 30 min, and then washed with PBS 3 times. Then, the cells were treated with Triton X-100 (0.1%, v/v, in PBS) for 30 min at room temperature and subsequently with goat serum (10%, v/v, in PBS) for 30 min at room temperature to reduce non-specific backgrounds. Following goat serum removal, the cells were treated with rabbit anti-human primary antibodies against Ki-67, p53, or HSP70 proteins (1:200 in 10%, v/v, goat serum, Sigma-Aldrich) for 2 h at room temperature. Then, thecells were gently washed with PBS 3 times before staining with a fluorescent goat anti-rabbit IgG secondary antibody (1:200 in 10%, v/v, goat serum, Invitrogen) and Hoechst (0.1%, v/v, in 10%, v/v, goat serum) for 30 min at room temperature. Images were acquired with the confocal scanning fluorescence
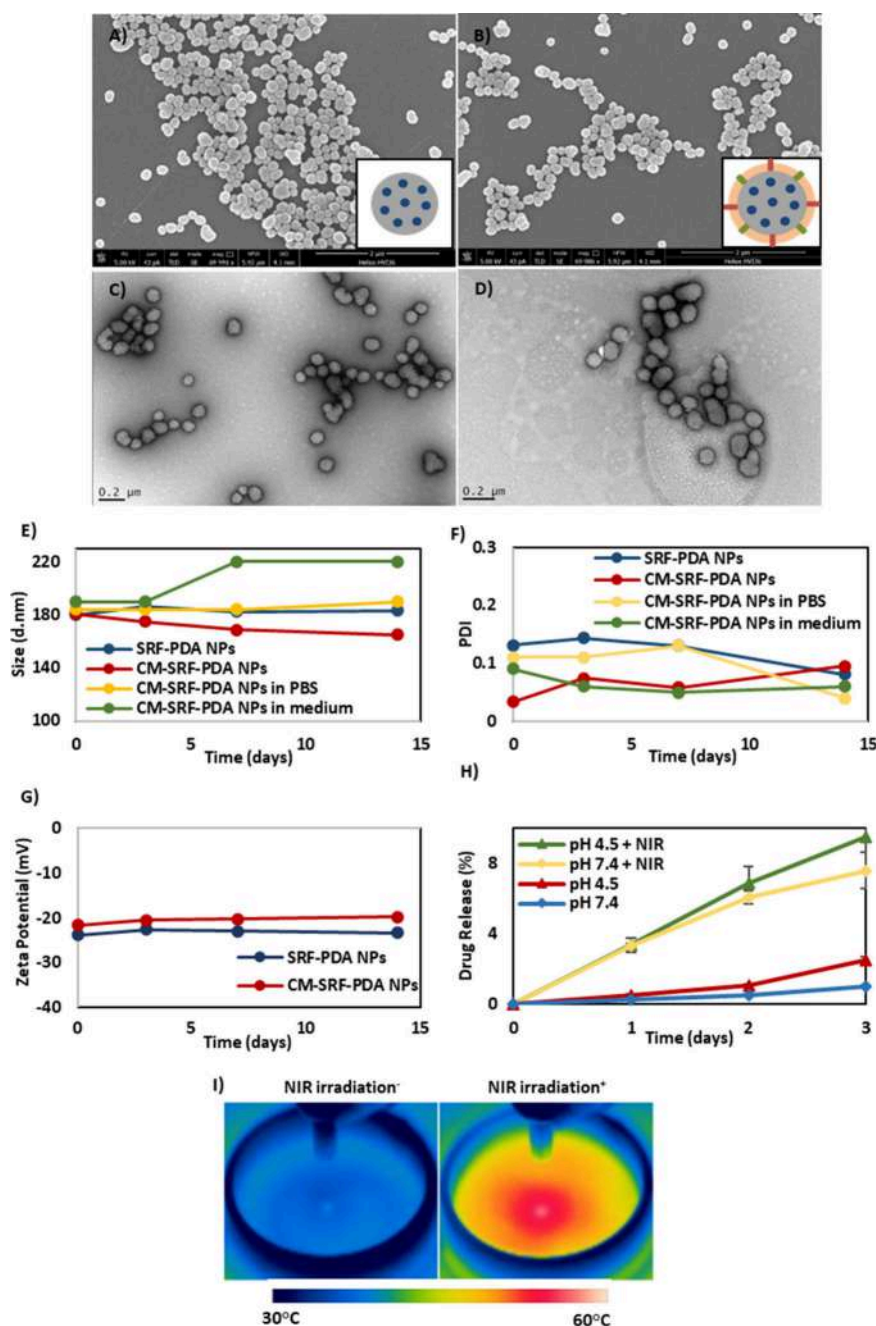
Figure 1. Representative (A and B) SEM and (C and D) TEM images of (A and C) SRF−PDA NPs and (B and D) CM−SRF−PDA NPs. (E) Hydrodynamic size, (F) polydispersity index, (G) ζ potential, and (H) drug release analyses. (I) Representative thermal camera images highlighting the photothermal conversion ability of CM−SRF−PDA NPs.

microscope (C2 system, Nikon); a minimum of 10 images were obtained from different areas of the cell cultures, and the number of the cells, positive for nucleus and marker staining, was calculated and analyzed with the ImageJ software.

2.10. Proteomic Analysis. For the proteomic analysis, HepG2 cells from the different experimental classes were lysed, reduced, and alkylated with LYSE buffer (50 μL, Preomics) at 95 °C for 10 min and sonicated (3 cycles, 30 s/cycle) with Ultrasonic Processor UP200St (Hielscher). Lysate samples were diluted 1:2 with 25 mM Tris at pH 8 and digested with 0.7 μg of trypsin and 0.3 μg of LysC overnight at 37 °C.

The resulting peptides were analyzed by a nano-ultra-high-performance liquid chromatography−tandem mass spectrometry (nano-UHPLC−MS/MS) system using an Ultimate 3000 RSLC coupled to an Orbitrap Q Exactive Plus mass spectrometer (Thermo

Scientific). Elution was performed with an EASY spray column (75 μm × 50 cm, 2 μm particle size, Thermo Scientific) at a flow rate of 250 nL/min using a linear gradient of 2−45% solution B [80% acetonitrile (ACN), 5% DMSO, and 0.1% formic acid (FA) in H$_2$O] in 50 min. Orbitrap detection was used for MS1 measurements at a resolving power of 70 000 in a range between m/z 375 and 1500 with a 3 × 10^6 automatic gain control (AGC) target and 50 ms maximum injection time (IT). Precursors were selected for data-independent fragmentation with an isolation window width of m/z 34 and a 19 loop count. Higher collisional dissociation (HCD) energy was set to 27%, and MS2 scans were acquired at a resolution of 35 000, 3 × 10^6 AGC target, and 50 ms maximum IT. All DIA raw files were processed with Spectronaut, version 18,[24] using a library-free approach (directDIA) under default settings. The library was generated against the UniProt Human database (release UP000005640_9606, November 2022). Carbami-

domethylation was selected as a fixed modification, and methionine oxidation N-terminal acetylation and deamidation (NQ) were selected as variable modifications. The false discovery rate (FDR) of peptide–spectrum match (PSM) and peptide/protein groups was set to 0.01. For quantification, precursor filtering was set to identified (Q value), and MS2 was chosen as the quantity MS level.

The Protein Quant Pivot Report generated by Spectronaut was statistically evaluated using Perseus software,[25] version 1.6.15.0. Gene ontology (GO) enrichment was obtained with the webserver HumanBase[26] with "liver" as the background.

2.11. Investigation of the Therapeutic Effect on 3D Cultures.
To prepare 3D cultures, 75 μL of a warm solution of agarose (1% in deionized water, Sigma-Aldrich) was added in each chamber of a 96-well plate to form a non-adherent round-bottom structure, after cooling for 10 min at room temperature. In each well, 10 000 HepG2 cells were seeded in 150 μL of medium. The plate was then centrifuged at 1500 rpm for 10 min; the half volume of the medium was changed every 2 days, followed by centrifugation at 1200 rpm for 5 min. Spheroids were collected after growth for 7 days of growth.

Nanoparticle internalization in the spheroids was analyzed following treatment with PDA NPs or CM–PDA NPs (100 μg/mL) for 24 h with confocal microscopy, as previously described.

The therapeutic efficiency of the nanovectors on the 3D cultures has been evaluated by considering the same experimental classes described for the 2D cultures and investigating apoptotic/necrotic phenomena after cell dissociation (trypsin treatment, 100 μL, 10 min of incubation at 37 °C). Flow cytometry analysis followed the procedure previously described. A qualitative morphological analysis of the spheroids was moreover performed following bright-field microscopy imaging.

2.12. *Ex Ovo* Chorioallantoic Membrane (CAM) Assay.
Fertilized eggs of Japanese quail (*Coturnix japonica*) were obtained from Japocaille (Saint Euphrône, France) and incubated at 37 °C on trays with an automatic rotator that turned eggs every 90 min with a humidity of 57%. The day eggs set in the incubator was considered embryonic day (ED) 6. At ED 9, the eggs were gently opened and the embryos were poured into a plastic weigh boat and transferred to a standard humidified incubator at 37 °C as shell-less culture. At ED 12, a small incision was performed with a 26G needle to open the CAM membrane. A HepG2 spheroid was placed on the incision with a pipette, and the embryo was returned to the incubator. Blood vessels vascularizing the spheroids were noticed within 1–2 days after grafting. At ED 13, 10 μL of CM–SRF–PDA NPs were directly placed on top of the tumor, at a concentration of 500 μg/mL, followed by 10 min of irradiation with a NIR laser at ED 14. Finally, the CAM-containing treated spheroids were fixed at ED 15 using 4% paraformaldehyde at 4 °C for 18 h. Samples were washed 4 times in PBS (1×) for 15 min each and immersed in 70% ethanol at 4 °C until further processing.

The fixed CAM samples were paraffin-embedded and cut into 5 μm thick sections, which were serially mounted on glasses. Immediately before use, slides were dewaxed, rehydrated, and processed for routine haematoxylin and eosin (H&E) staining. Briefly, sections were stained with Mayer haematoxylin solution (Kaltek) for 5 min; after 10 min under running tap water, samples were counterstained with 1% eosin aqueous solution (Kaltek) for 1 min. After a brief washing in water, sections were dehydrated, clarified, and mounted by Bio Mount HM (Bio-Optica). Specimens were observed by a BX43 light microscope (EVIDENT Europe GmbH), and images were captured at 400× total magnification (40× objective magnification and 10× ocular magnification) by a DP28 digital camera (EVIDENT Europe GmbH).

2.13. Statistical Analysis.
Statistical analysis was performed using analysis of variance (ANOVA) followed by Bonferroni's post-hoc test. The significance was set at $p < 0.05$, and data were presented as the mean value ± standard deviation of three independent experiments.

3. RESULTS AND DISCUSSION

3.1. Nanoparticle Characterization.
Nanoparticles were obtained by self-polymerization of dopamine, with a production yield of 27.4 ± 1.3%. Effective polymerization has been confirmed by Raman spectroscopy (Figure S3 of the Supporting Information); the dopamine hydrochloride spectrum shows peaks typical of aliphatic chains (600–1300 cm^{-1}) and matched that provided by the supplier (H8502, Sigma-Aldrich). The Raman spectrum of PDA NPs shows instead bands at 1350 and 1580 cm^{-1}, typical of aliphatic and aromatic components and coherent with polydopamine spectra provided by the literature.[27]

Morphological characterization of SRF–PDA NPs and CM–SRF–PDA NPs was performed by SEM (panels A and B of Figure 1, respectively; the inset represents a schema of the nanovectors) and TEM (panels C and D of Figure 1, respectively). The images demonstrate highly uniform and spherical nanostructures, also maintained after the coating with the cell membrane. The average hydrodynamic size did not show any relevant change along 14 days of incubation and, at the end of this analysis period, resulted in 182.9 ± 2.6 nm for SRF–PDA NPs and 172.3 ± 6.9 nm for CM–SRF–PDA NPs in water, while resulting in 185.5 ± 3.0 and 220.0 ± 4.2 nm for CM–SRF–PDA NPs in PBS and cell complete medium, respectively (Figure 1E); the uniform size distribution is moreover confirmed by the polydispersity index (PDI of <0.2 up to 14 days of assessment; Figure 1F). The ζ potential resulted in −23.2 ± 0.5 mV for SRF–PDA NPs and −20.5 ± 0.7 mV for CM–SRF–PDA NPs, again without any substantial change along the 14 day observation window (Figure 1G), further supporting the good colloidal stability of the obtained nanoparticles.

Concerning drug encapsulation, the LC and EE of CM–SRF–PDA NPs were found to be 2.3% (w/w) and 45.5 ± 0.6%, respectively. The SRF release profile from CM–SRF–PDA NPs at different time points (0, 24, 48, and 72 h) and different pH values (pH 7.4 and 4.5) in either the presence or absence of NIR stimulation (10 min/day, at 0.541 W/cm^2) is reported in Figure 1H. At the end point of observation (72 h), 2.5 ± 0.2% (without NIR) and 9.48 ± 0.9% (with NIR) of SRF was released at pH 4.5, while 1.0 ± 0.0% (without NIR) and 7.6 ± 1.0% (with NIR) was released at pH 7.4, suggesting a NIR-triggered release in both conditions.

To evaluate the NIR responsiveness, an aqueous dispersion of CM–SRF–PDA NPs (100 μg/mL), stabilized at an initial temperature of 37 °C, underwent a 10 min NIR light irradiation (808 nm, at 0.541 W/cm^2). The temperature, measured with a thermal camera, increased up to 54 ± 2°C, suggesting excellent photothermal conversion capacity of the nanoparticles. This phenomenon has been associated with the light absorption of polydopamine in the NIR region of light; however, the precise physical mechanism behind the conversion to heat remains poorly described.[28] Many studies have already demonstrated that PDNPs act as excellent NIR photothermal conversion agents, even with respect to traditional inorganic nanoparticles.[29] In extensive research conducted by our group, the size-dependent photothermal conversion capacity of the PDA NPs was investigated using a library of eight nanoparticles with different sizes, ranging from 145 to 957 nm diameter, demonstrating a 51% temperature increment difference between the largest and smallest nanoparticles.[19]

X-ray photoelectron spectroscopy (XPS) analysis of SRF–PDA NPs and CM–SRF–PDA NPs was used to identify the chemical composition of the nanostructure surface by detecting the present elements (C, N, O, and P) and their chemical environment by looking at the binding energy of the corresponding XPS signals. Nitrogen and oxygen contents were found higher in the CM–SRF–PDA NP samples, most
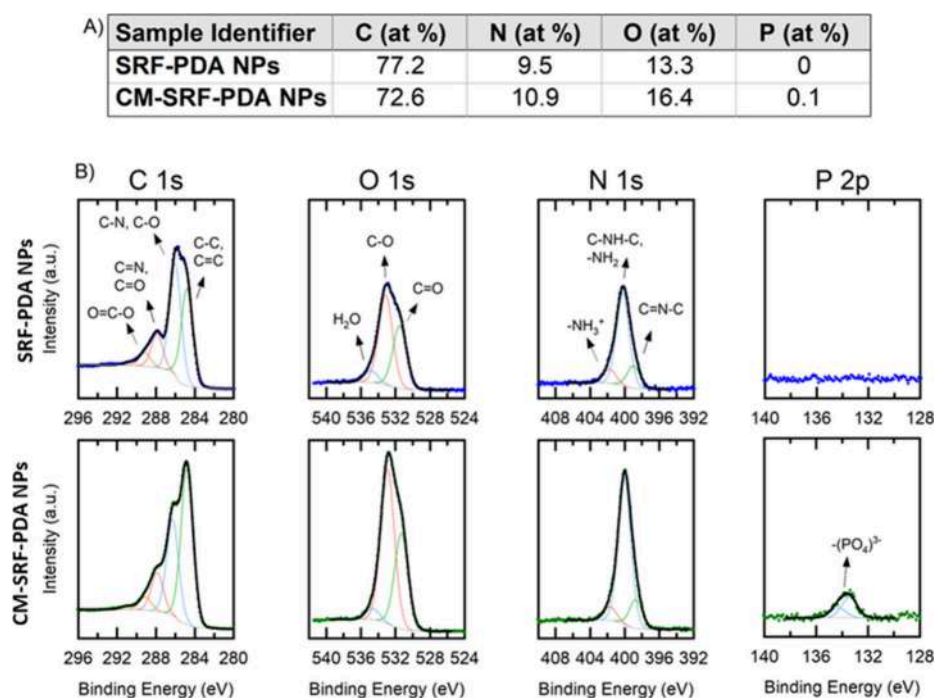
Figure 2. High-resolution XPS analysis of SRF−PDA NPs and CM−SRF−PDA NPs. (A) Percentage of element content and (B) energy binding spectra of C 1s, O 1s, N 1s, and P 2p.

likely because of the presence of the cellular membrane (Figure 2A).[30] The literature supports this finding, as increased N and O contents have been found in trypsin-functionalized PDA films, by exploiting interactions between the catechol or quinone units of PDA with nucleophile groups of histidine of trypsin.[31] The high-resolution (Figure 2B) C 1s spectra of both samples were decomposed into five components centered at 284.8 ± 0.2, 286.1 ± 0.2, 287.9 ± 0.2, 289.1 ± 0.2, and 290.8 ± 0.2 eV, which are assigned to C−C, C−N and C−O, C=O and C=N, and O=C−O bonds and a shake-up peak, respectively.[32] Concerning the O 1s spectrum, the observed signal can be decomposed for both samples into three peaks, centered at 531.4 ± 0.2, 533.0 ± 0.2, and 534.7 ± 0.2 eV, corresponding to O=C, O−C, and adsorbed water, respectively.[33] Slight increments in the intensity of O−C and O=C peaks in CM−SRF−PDA NPs can be attributed to the high content of these groups in the glycerophospholipids present in the cell membranes. The N 1s spectrum was decomposed into three peaks centered at 398.9 ± 0.2, 400.1 ± 0.2, and 401.7 ± 0.2 eV, attributed to imine N (C=N−C), secondary amine moieties (C−NH−C), and protonated amines, respectively.[32]

A potential interaction between polydopamine and the cell membrane could occur between the zwitterionic phospholipids in the cell membrane with the amine, catechol, and quinone groups of polydopamine, negatively charged at physiological pH as a result of the deprotonation of the catechol group. In this regard, P 2p signals, for which each chemical state is characterized by a doublet of peaks as a result of spin-orbit splitting, were found centered at 133.4 and 134.0 eV only in CM−SRF−PDA NPs but not SRF−PDA NPs. The observed signal is compatible with the presence of phosphates, and this result supports the presence of cell membranes in CM−SRF−PDA NPs, because the glycerophospholipids, the main component of the cell membrane, contain phosphate groups in their backbone.[34]

3.2. Cell/Nanoparticle Interaction. Cytocompatibility evaluation was performed upon treatment with PDA NPs, SRF, CM−PDA NPs, or CM−SRF−PDA NPs, by assessing both the cell metabolic activity and viability (Figure S4 of the Supporting Information). According to the obtained results, after 24 h of incubation with the highest concentrations of SRF, the metabolic activity of cells was significantly reduced (76.3 ± 3.8% for 0.230 μg/mL, corresponding to the concentration loaded in 100 μg/mL CM−SRF−PDA NPs, and 70.4 ± 4.4% for 0.575 μg/mL, corresponding to the concentration loaded in 250 μg/mL CM−SRF−PDA NPs). Concerning CM−SRF−PDA NPs, the reduction was up to 87.5 ± 1.1% for the 100 μg/mL treatment while 80.3 ± 8.5% after the 250 μg/mL treatment (in all cases, $p < 0.05$ with respect to the control groups). After 72 h, such reduction occurred also starting from 0.057 μg/mL SRF (86.4 ± 1.4%); in the case of CM−SRF−PDA NPs, a significant metabolic activity reduction occurred since 100 μg/mL (86.5 ± 0.5%; panels A and B of Figure S4 of the Supporting Information). Similar results were obtained in terms of cell viability (panels C and D of Figure S4 of the Supporting Information).

Analogous drug effects can be found in the literature; as an example, a study devoted to the investigation of the therapeutic activity of SRF-loaded polymeric nanoparticles showed a dose-dependent growth inhibitory effect on H22 HCC cells, reducing cell viability up to 54.1 ± 1.5%.[35] These results indeed confirm the optimal biocompatibility of PDA-based nanostructures up to very high doses; considering a compromise between drug effects and the nanovector concentration safety threshold, the working CM−SRF−PDA NP concentration for the following tests was set at 100 μg/mL.

Homotypic cellular targeting has been investigated on HepG2 cells by monitoring the intracellular NP content using confocal microscopy, and representative results are reported in Figure 3A. These images suggest the intracellular NP accumulation and diffusion in the cytosol and perinuclear area of the cells.

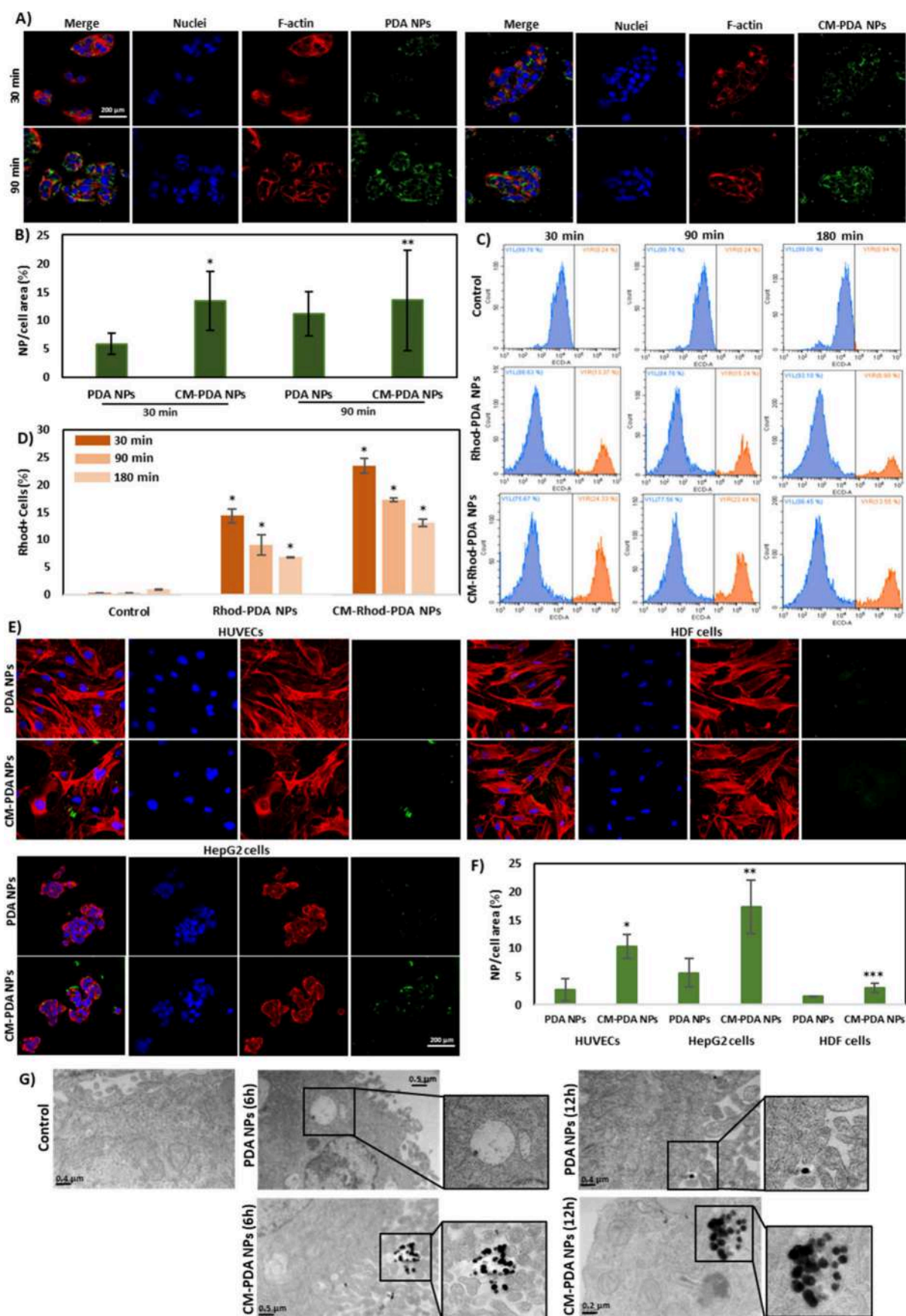**Figure 3.** (A and B) Representative confocal images and (C) quantitative analysis of (A) PDA NP and (B) CM−PDA NP internalization by HepG2 cells (nuclei in blue, *f*-actin in red, and nanoparticles in green). (D) Representative flow cytometry scatter plots and (E) quantitative analysis of internalization analysis on HepG2 cells treated with Rhod−PDA NPs or CM−Rhod−PDA NPs. (F) Representative confocal images and (G)

Figure 3. continued

quantitative analysis of internalization investigation in dynamic conditions on HMECs, HDFs, and HepG2 cells treated with PDA NPs or CM−PDA NPs (nuclei in blue, *f*-actin in red, and nanoparticles in green). (H) Representative TEM images of the HepG2 cells treated with PDA NPs or CM−PDA NPs, with the control reported as well. In panels C, E, and F, data were represented as mean values ± standard deviation (∗, $p < 0.05$; ∗∗, $p < 0.01$; ∗∗∗, $p < 0.005$; $n = 3$).

Quantitative analysis has also been performed in terms of NP/cell percent area (Figure 3B), and data highlighted a higher uptake extent of CM−PDA NPs (13.4 ± 5.2% at 30 min and 13.5 ± 8.8% at 90 min) with respect to PDA NPs (5.9 ± 1.8% at 30 min and 11.2 ± 3.9% at 90 min), providing a first hint of a relevant contribution of cell membrane coating in the internalization mechanisms.

The cellular internalization of the nanostructures has also been quantitatively evaluated by flow cytometry analysis by exploiting rhodamine-123-stained nanostructures (Rhod−PDA NPs and CM−Rhod−PDA NPs; an extensive characterization of these nanostructures is reported in panels A and B of Figure S5 of the Supporting Information). Representative scatter plots are reported in Figure 3C, while the quantitative analysis is in Figure 3D. Obtained results indicate that the CM−Rhod−PDA NPs are internalized at a higher extent at each time point (23.4 ± 1.3, 17.3 ± 0.4, and 13.1 ± 0.7% of NP-positive cells after 30, 90, and 180 min of incubation, respectively) with respect to Rhod−PDA NPs (14.3 ± 1.3, 9.0 ± 1.9, and 6.9 ± 0.1% after 30, 90, and 180 min of incubation, respectively). These data confirm a preferential uptake of cell-membrane-coated nanostructures by HepG2 cells, corroborating the achievement of a successful homotypic internalization process.

To highlight that in the flow cytometry analysis, we detected a time-dependent reduction of the fluorescent signals in all cell cultures treated with either Rhod−PDA NPs or CM−Rhod−PDA NPs. We hypothesized that this outcome may be due to quenching phenomena deriving from a high uptake extent and a consequent aggregation of nanoparticles in the cell cytoplasm, as already suggested in the literature.[36]

The selective targeting of CM−PDA NPs has also been evaluated in dynamic conditions by exploiting a multi-compartmental microfluidic system comprising different cell lines (HUVECs, HepG2, and HDFs). The behavior of the CM−PDA NPs in such a simple model of multiple tissues provides significant information about their accumulation in different districts, thus suggesting the extent of possible side effects of the proposed therapeutic approach. HUVECs, HepG2 cells, and HDFs were separately seeded in the chambers of the bioreactor, where a 200 μg/mL dispersion (in medium) of nanoparticles (either PDA NPs or CM−PDA NPs) was administered at a flow rate of 2.5 μL/min for 1 h. The cellular uptake was comparatively evaluated by confocal acquisitions at the end of the experiment (Figure 3E) and consequent evaluation of the NP/cell percent areas (Figure 3F). Overall, it has been found that the cellular internalization of CM−PDA NPs was higher with respect to that of the PDA NPs in all of the considered cell lines; however, the most relevant result was a significantly higher uptake of CM−PDA NPs by HepG2 cells with respect to the other cell lines, confirming a selective internalization mediated by homotypic targeting. These data are not surprising, and similar results have already been achieved by our group, for example, in the case of selective targeting of nanoparticles toward glioma cells.[18,20] A selective and specific targeting is of paramount importance in view of pre-clinical translation, because it contributes to reduce

off-target drug accumulation and, thus, side effects, particularly heavy in the case of SRF.[37]

TEM images of the HepG2 cells, treated with either PDA NPs or CM−PDA NPs, were eventually acquired after 6 and 12 h of incubation to have a more in-depth characterization of internalization and intracellular localization (Figure 3G). After 6 h of incubation, PDA NPs were detected just outside the cell; conversely, CM−PDA NPs already approached the cell membranes and, in many cases, were already found in intracellular vesicle-like structures. After 12 h of incubation, PDA NPs have also been observed in intracellular vesicles, potentially endosomes. Eventually, CM−PDA NPs have been observed at a qualitatively higher extent inside cells after 12 h of incubation, and their endosomal accumulation provides a hint about potential receptor-mediated endocytosis, as also reported in other studies.[38] It is worth highlighting that no ultrastructural changes in nanoparticle-treated cells with respect to control cultures were found, once more confirming the high biocompatibility of these nanostructures.

The photothermal conversion capacity of the nanostructures internalized by cells was indirectly measured during NIR light stimulation (10 min, at 0.541 W/cm^2) by exploiting nanoparticle functionalization with a temperature-sensitive dye (DiI). Figure 4A shows confocal acquisitions highlighting a
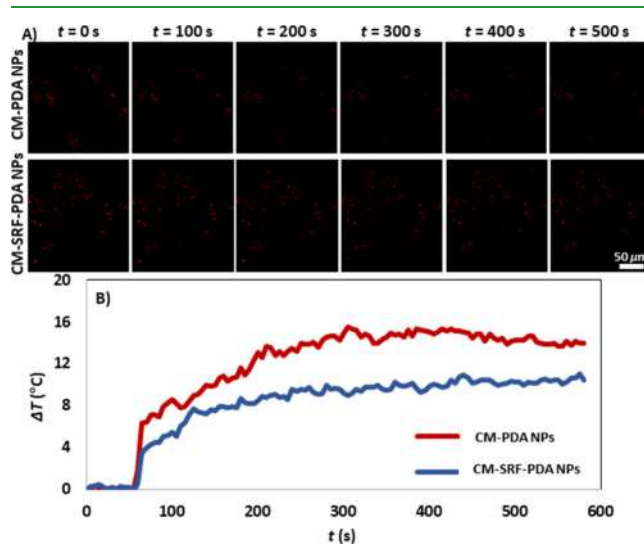

Figure 4. Intracellular temperature assessment: (A) representative confocal microscopy images and (B) quantitative evaluation.

decrement of the fluorescence intensity, quantified and converted into an increment of temperature based on a calibration curve ($\Delta F/F_0 = -0.0224\Delta T$; $R^2 = 0.99$[23]). Figure 4B reports the temperature trend in the case of a 10 min NIR stimulation in the presence of both CM−PDA and CM−SRF−PDA NPs: a maximum increment of $\Delta T = 14.8 \pm 2.4$ °C was recorded in the presence of CM−SRF−PDA NPs, with $\Delta T = 9.8 \pm 3.1$ °C in the presence of CM−PDA NPs. The obtained results show that the nanostructures present a significant
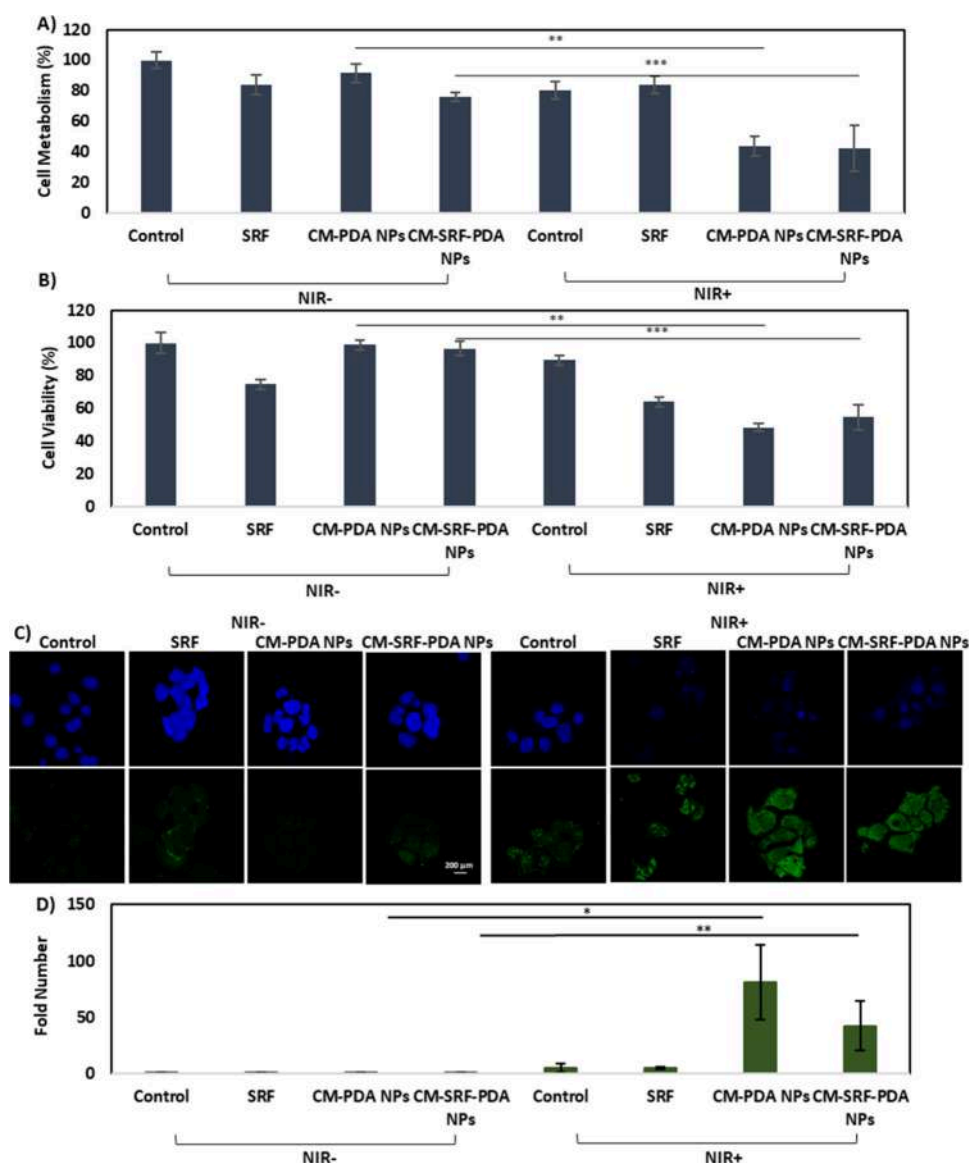
Figure 5. (A) Metabolic activity and (B) proliferation evaluation in the considered experimental classes. HSP70 expression: (C) representative confocal microscopy images (nuclei in blue and HSP70 in green) and (D) quantitative evaluation. Data are represented as mean values ± standard deviation (∗, $p < 0.05$; ∗∗, $p < 0.01$; ∗∗∗, $p < 0.005$; $n = 3$).

intracellular photothermal conversion ability, indeed adequate for hyperthermal stimulation.[19] The difference observed between unloaded and drug-loaded nanoparticles can be attributed to a size difference of the nanoparticles (205.1 ± 7.3 nm for CM−PDA NPS and 172.3 ± 6.9 nm for CM−SRF−PDA NPs); in fact, as reported by previous work from our group, a direct correlation between the nanoparticle size and photothermal conversion can be described,[19] with larger nanoparticles acting as better transducers in terms of heat generation.

3.3. Therapeutic Effects on 2D Cultures. Once the ability of the nanoparticles to intracellularly increase the temperature upon NIR illumination was assessed, therapeutic effects have been assessed in terms of metabolic activity, proliferation, and HSP70 expression. The experiments were performed following the treatment of cells with SRF, CM−PDA NPs, or CM−SRF−PDA NPs in either the presence or absence of NIR stimulation (3 days, 10 min/day, at 0.541 W/cm^2); control experimental classes have been considered as well. Figure 5A shows that the metabolic activity of CM−PDA NP and CM−SRF−PDA NP-

treated cells significantly decreased in the presence of NIR stimulation (43.6 ± 6.6 and 42.3 ± 15.1%, respectively) with respect to non-illuminated cultures (91.4 ± 6.1 and 75.8 ± 2.9%, respectively). An analogous situation was found when cell viability was considered (Figure 5B): also, a significant reduction was found in the case of NIR stimulation (48.3 ± 7.7 and 54.4 ± 2.2% for CM−PDA NP- and CM−SRF−PDA NP-treated cells, respectively) with respect to non-stimulated cells (98.8 ± 3.0 and 96.4 ± 4.3%, respectively). It is also worth highlighting that SRF treatment induced a slight reduction in terms of both metabolic activity and proliferation independent of NIR stimulation.

The HSP protein family comprises molecular chaperones expressed as a response to cellular stress; they bind to specific substrate proteins to stabilize them against denaturation and aggregation occurring under stress conditions. The overexpression of HSP70 protein is thus associated with an increased cell stress level, potentially stimulated by adverse environmental conditions, such as a high temperature, loss of water, and
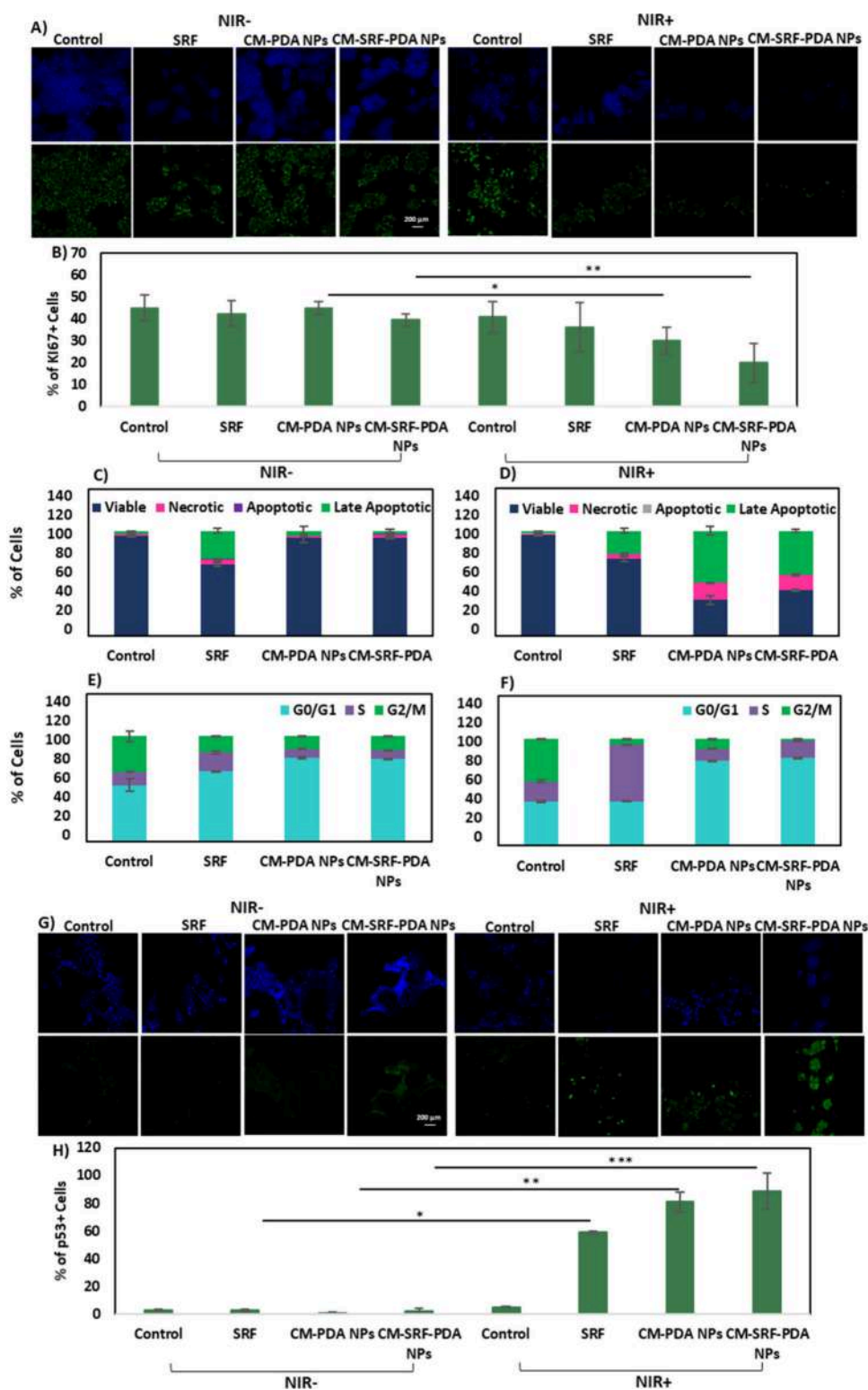
Figure 6. Evaluation of the therapeutic effects. Ki-67 protein expression analysis: (A) representative immune fluorescence images (nuclei in blue and Ki67 in green) and (B) quantitative analysis. Flow cytometry analysis of necrotic, apoptotic, late apoptotic, and alive cells (C) without and (D) with NIR stimulation. Cell cycle analysis (E) without and (F) with NIR stimulation. p53 protein expression analysis: (G) representative immune fluorescence images (nuclei in blue and p53 in green) and (H) quantitative analysis. Data are represented as mean values ± standard deviation ($*$, $p <$ 0.05; $**$, $p < 0.01$; $***$, $p < 0.005$; $n = 3$).

excessive drug exposure.[39] It is thus clear that HSP70 expression investigation can provide important clues about the stress level of HepG2 cells treated according to the previously described treatment protocols. Figure 5C shows representative confocal

images following immune staining against HSP70, while Figure 5D reports a quantitative analysis. The expression of HSP70 was significantly increased in the NIR⁺ experimental classes in the presence of nanoparticles: 81.2 ± 32.9 (CM−PDA NPs) and

41.9 ± 21.9 (CM−SRF−PDA NPs) fold versus 0.6 ± 0.4 (CM−PDA NPs) and 0.3 ± 0.2 (CM−SRF−PDA NPs) fold without NIR stimulation. Considering the SRF treatment, the HSP70 expression slightly increased independently from NIR stimulation, suggesting moderate drug-induced cellular stress.

The Ki-67 protein is present in the nucleus of actively proliferating cells, and it is widely considered a marker of tumor cell growth and an indicator of anti-cancer therapy efficiency.[40] Figure 6A shows representative confocal images of cultures that underwent the already described treatments acquired after immune staining of Ki-67. A reduction of protein expression was clear in the CM−PDA NP and CM−SRF−PDA NP experimental classes following NIR irradiation. From the same images, moreover, it has been possible to appreciate an evident decrement of the cell number in the treatments with SRF (with and without NIR stimulation), CM−PDA NPs + NIR, and CM−SRF−PDA NPs + NIR. The quantitative analysis (Figure 6B) confirms the qualitative evidence: we could find 30.1 ± 5.9% of Ki-67$^+$ cells in the case of CM−PDA NPs + NIR and 19.9 ± 8.8% in the case of CM−SRF−PDA NPs + NIR, while all of the other experimental classes presented about 40% of Ki-67$^+$ cells. These data demonstrate an important inhibition of cell proliferation following the proposed therapeutic approach.

HCC development is strictly related to the overexpression of many proteins that play critical roles in hindering the apoptotic cascade, such as Bcl-2, Bcl-xL, and Mcl-1. SRF has been demonstrated to induce apoptosis by downregulating the Bcl-2 family proteins in the HepG2 cells.[41] Another study also demonstrated that the occurrence of nuclear condensation and fragmentation in HepG2 cells is directly related to the dose of administered SRF.[42] On the other side, hyperthermia also initiates apoptotic or necrotic phenomena, depending upon the extent of temperature increment: apoptosis occurs in case the temperature reaches a range of 41−47 °C, while necrosis occurs by heat shock in case of protein denaturation at temperatures higher than 50 °C.[43] Other studies also showed that SRF induces intrinsic apoptosis by leading to mitochondrial dysfunction and adenosine triphosphate (ATP) level decrease via mitochondrial translocation of Bax and release of cytochrome *c*.[44]

Apoptotic and necrotic responses of the cells following the treatment with SRF, CM−PDA NPs, or CM−SRF−PDA NPs were evaluated in either the absence or presence of NIR irradiation, as shown in panels C and D of Figure 6 (representative data in Figure S6A of the Supporting Information). The SRF treatment induced late apoptosis in 27.0 ± 2.7 and 21.9 ± 1.8% of cells in the absence and presence of NIR irradiation, respectively. In the case of NIR stimulation, the treatment with CM−PDA NPs and CM−SRF−PDA NPs induced necrosis in 16.4 ± 1.3 and 14.7 ± 0.2% of the cells as well as late apoptosis at 49.6 ± 2.0 and 41.8 ± 3.5% of the cells, respectively; the cells indeed were exposed to a temperature high enough to induce both necrosis and apoptosis (please check panels A and B of Figure 4). The significant percentage of both apoptotic and necrotic cells suggests different extents of temperature increments in the cultures, even within the same experimental class; however, we cannot exclude a direct effect of a high temperature on apoptosis promotion, for example, by upregulated heat-shock proteins like Fas ligand (FasL).[45]

Distribution of HepG2 cells in various proliferative cycle phases, following the different treatment protocols, is reported in panels E and F of Figure 6 (representative data in Figure S6B of the Supporting Information). SRF slightly increased the percentage of the cells in G0/G1 and S phases (from 50.9 ± 5.4

to 63.1 ± 0.1% and from 12.2 ± 0.6 to 17.1 ± 1.2%, respectively), while the percentage of the cells in the G2/M phase was reduced (from 32.6 ± 5.5 to 14.7 ± 0.2%), with respect to the NIR$^-$ control group. Considering the results obtained after NIR irradiation, the cells in the S phase significantly increased (from 18.1 ± 1.7 to 51.6 ± 0.3%), while the cells in the G2/M phase reduced from (5.2 ± 0.2 to 38.0 ± 0.2%), with respect to the NIR$^+$ control group. SRF, as a tyrosine kinase inhibitor, is known to lead to cell cycle arrest; with this considered, the increment of the cells in the G0/G1 and S phases following SRF treatment can be attributed to the fact that a high percentage of cells are in these phases before drug administration, and the latter induces the same cells to remain in that status.[46] On the other side, light between 710 and 1100 nm is absorbed by complexes of the electron transport chain (ETC) of mitochondria; this is indeed hypothesized to potentially (i) elevate reactive oxygen species (ROS) production and (ii) enhance ETC function, thus increasing ATP production.[47] This phenomenon could explain the increase in cells in the S phase following the SRF + NIR treatment mediated by NIR irradiation and a consequent arrest in the S phase caused by SRF.

Considering NIR stimulation in the presence of nanoparticle cultures treated with CM−PDA NPs and CM−SRF−PDA NPs showed a significant reduction of the G2/M phase (from 11.9 ± 0.0 to 9.02 ± 0.4% and from 12.6 ± 0.2 to 1.5 ± 0.1%, respectively) and an increment of the S phase (from 7.6 ± 0.4 to 11.0 ± 0.4% and from 8.2 ± 0.2 to 15.5 ± 0.7%, respectively). High temperatures affect the cell cycle phases at different extents, and indeed G2/M > S > G0/G1. The highest sensitivity of cells occurs in the G2/M phase because the high temperature causes irreversible damage to the mitotic apparatus; however, the cells are less sensitive to heat in the S phase and show maximal resistance in the G0/G1 phase.[48] This can explain the higher percentage of cells in the G0/G1 phase following NIR irradiation.

The p53 apoptosis marker expression in HepG2 cells was analyzed, and as presented in the representative images in Figure 6G, it was significantly high in the CM−PDA NPs + NIR and CM−SRF−PDA NPs + NIR experimental groups. The quantitative analysis (Figure 6H) provided that, following NIR stimulation, p53$^+$ cells in SRF + NIR, CM−PDA NPs + NIR, and CM−SRF−PDA NPs + NIR groups (58.8 ± 0.9, 80.8 ± 7.3, and 88.1 ± 13.1%, interestingly, also in the absence of nanoparticles, in the "plain" SRF + NIR treatment), respectively, were significantly higher with respect to the respective NIR$^-$ experimental classes (2.5 ± 0.5, 0.7 ± 0.5, and 1.9 ± 1.7%, respectively). The p53 protein is located in the nucleus of the cells, where it binds to DNA regulating cell division and hindering it in the case of any unfavorable situation, thus acting as a tumor suppressor protein. Some evidence shows that a p53-triggered pathway promotes the cell cycle arrest in the G0/G1 phase and initiates apoptotic response.[49] This is in line with our findings, showing that the arrest in the G0/G1 phase and the apoptotic response in the CM−PDA NPs + NIR and CM−SRF−PDA NPs + NIR experimental groups are probably triggered by a p53 overexpression.

3.4. Proteomics. The response of HCC cells to the already widely described treatments (control, SRF, CM−PDA NPs, and CM−SRF−PDA NPs in either the presence or absence of NIR stimulation) has also been analyzed through proteomics, and the most important comparisons are depicted in Figure 7 and commented on in the following.
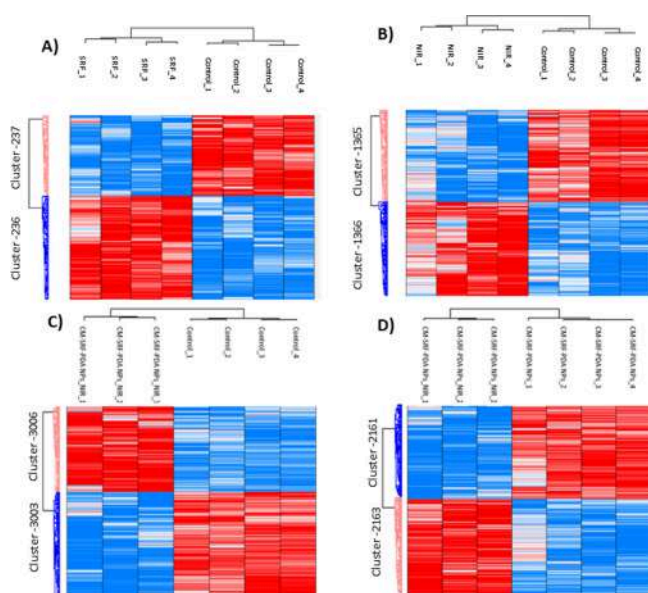
Figure 7. Heatmaps showing differential expression of proteins in some representative comparisons. (A) SOR versus the control, (B) NIR versus the control, (C) CM−SRF−PDA NPs + NIR versus the control, and (D) CM−SRF−PDA NPs + NIR versus CM−SRF−PDA NPs.

SRF treatment (Figure 7A) induced the overexpression of β-arrestin-1 (ARRB1), which interacts with G-protein-coupled receptors (GPCRs) to mediate their internalization and desensitization. Recent studies indicate that ARRB1 promotes DNA damage and cell apoptosis: this property may enhance ARRB-dependent chemosensitivity,[50] confirming our observations in the analysis of the cell death mechanism (Figure 6C). A downregulation was found concerning the ubiquitination of UBE2A protein, a member of an E2 enzyme group. This protein belongs to a major DNA damage repair system and is recognized as a controller of numerous physiological processes, including cell cycle progression and cell survival. UBE2A is a regulator of G1/S transition and proliferation in cells by targeting the cyclin D1 expression.[51] Its downregulation in the case of SRF treatment is attributed to the therapeutic effect of the drug. Continuing with the analysis of the differently expressed proteins, we found a downregulation of the E2 protease. This protein is involved in the degradation of HSP-dependent misfolded proteins and, in particular, those marked for ubiquitination by HSP70 and HSP90.[52] The downregulation of the E2 protease causes the accumulation of ubiquitinated proteins, thus triggering apoptosis. This finding is in line with the already described overexpression of HSP70 (panels C and D of Figure 5) and stimulated apoptotic response in the case of SRF treatment (panels C and D of Figure 6).[53] Eventually, the serine protease 1 (PRSS1) was found downregulated in SRF-treated cells; considering the oncogenic activity of this protein, its downregulation inhibits the ERK signaling pathway, resulting in weakened growth and proliferation of HCC, in line with the SRF therapeutic activity.[54]

Light in the spectral range from red to NIR (630−1000 nm) accelerates wound healing, improves recovery from ischemic injuries in the heart, and attenuates degeneration in injured optic nerves. Tissue recovery occurs thanks to the activation of mitochondrial respiratory chain components; particularly, cytochrome oxidase is a key photoacceptor for NIR light, triggering a signaling cascade that promotes cellular proliferation

and protection.[55] In our study, NIR light treatment (Figure 7B) induced a reduction of expression of some proteins, for example, myosin Vc (MYO5C), a protein mainly involved in cell motility, vesicular trafficking, and the intracellular transport of macromolecules based on movements of the actin filaments driven by ATP hydrolysis.[56] The downregulation of MYO5C expression is attributed to the NIR-dependent impaired motility and vesicle traffic in HCC cells. Following NIR irradiation, nucleolar protein ERCC3, also named XPB, was found instead of overexpressed. This protein is involved in the DNA damage response, modulating DNA damage repair through the DNA repair factor TFIIH helicase. Moreover, XPB is considered one of the targets of p53 to stimulate apoptosis.[57] Overexpressed ERCC3 may thus promote DNA repair and apoptosis, suggesting an association between NIR treatment and the inhibition of tumor development.

Moving to the effects induced by the CM−SRF−PDA NPs + NIR treatment (Figure 7C), Trem-like transcript 2 (TREML2) protein overexpression has been detected. TREML2 suppresses HCC oncogenesis and metastasis by inhibiting epithelial−mesenchymal transition, accompanied by abnormal expression of epithelial and mesenchymal markers by targeting the PI3K/Akt/β-catenin pathway.[58] Analogously, the ubiquitin-like ring finger domain 1 (UHRF1) protein was found to be downregulated. This protein is expressed to a high extent in HCC and is significantly correlated with cell proliferation and metastasis. The downregulation of UHRF1, seen in the case of CM−SRF−PDA NPs + NIR treatment, is associated with G2/M cell cycle arrest and inhibition of cell proliferation and aggressiveness.[59]

Considering the comparison of CM−SRF−PDA NPs + NIR versus CM−SRF−PDA NPs (Figure 7D), an overexpression of the transcription initiation factor TFIID subunit 5 (TAF5) was found. The transcription of genes by RNA polymerase II may require a transcription preinitiation complex (TFIID), which includes the TATA sequence binding factor (TBP) and TBP-associated factors (TAFs).[60] TAFs are composed of several subunits that participate in basal transcription by serving as co-activators, functioning in the recognition of promoters, or modifying general transcription factors (GTFs) to facilitate complex assembly and transcription initiation. TAF5 can recognize and bind to downstream promoters as well as interact with transcriptional activators. A study shows a strong interaction between TAF5 and AF9 proteins, which play a significant role in pro-apoptotic transcription.[61] With this all considered, the overexpression of TAF5 implies a pro-apoptotic transcription program initiating the apoptotic cascade following CM−SRF−PDA NPs + NIR treatment. The overexpression of another TAF protein (TAF1C) in the cells treated with CM−PDA NPs and stimulated with NIR is a further hint of apoptotic phenomena. The Fanconi Anemia Group G (FANCG) protein participates in DNA damage response, which induces DNA damage sensitivity and apoptotic response.[62] Its overexpression thus contributes to the induction of the apoptotic response following hyperthermia-mediated DNA damage in HCC cells. An oncogene protein, chromodomain helicase DNA-binding 4 (CHD4), was found downregulated; loss of the CHD4 function can sensitize tumor cells to oxidative damage and promote genome stability by helping to regulate p53-dependent cell cycle checkpoints.[63] A chromatin target of the PRMT1 protein (CHTOP) was instead found to be overexpressed. This protein stimulates the tumor suppressor function of p14^{ARF} by methylating several arginine residues in the C-terminal nuclear/nucleolar localization sequence. Considering the
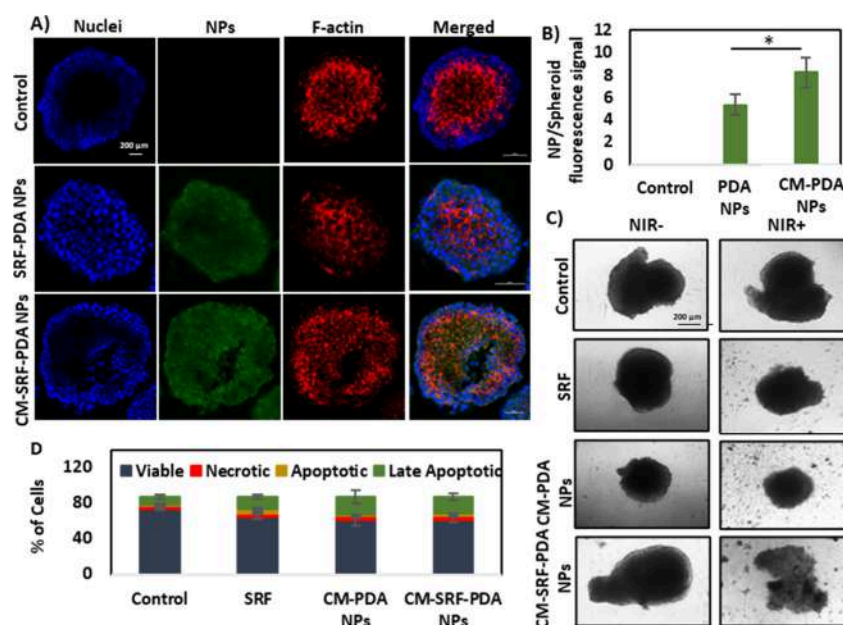
Figure 8. (A) Representative confocal images and (B) quantitative analysis of PDA NP and CM−PDA NP internalization by 3D HepG2 spheroids (nuclei in blue, *f*-actin in red, and nanoparticles in green). (C) Representative bright-field microscopy images of spheroids that underent the different experimental treatments. (D) Flow cytometry analysis of necrotic, apoptotic, late apoptotic, and alive cells following NIR stimulation. Data are represented as mean values ± standard deviation (∗, $p < 0.05$; $n = 3$).

p14[ARF] p53-dependent and p53-independent tumor-suppressive activities, CHTOP protein overexpression plays an important role in the apoptosis of HCC cells.[64]

In conclusion, the performed comparative proteomic analysis demonstrates that chemotherapy and hyperthermia concur in the activation of several and complementary pathways leading to cancer cell apoptosis and proliferation inhibition.

3.5. Therapeutic Effects on 3D Cultures. In view of future *in vivo* applications, where indeed we have to face some particular physiological conditions of the tumor, such as hypoxia, nutrient deficiency, and the presence of a compact structure that potentially causes difficulties in the transport through the center of the tumor, in the present study, we made a step forward with respect to simple 2D testing, by introducing experiments on HepG2-derived spheroids that represent a relatively more tumor microenvironment-mimicking condition.

The diffusion profile of either SRF−PDA NPs or CM−SRF−PDA NPs through the center of the spheroids was qualitatively evaluated by confocal microscopy, as depicted by the representative images in Figure 8A. The images show an intensive internalization and distribution of both SRF−PDA NPs and CM−SRF−PDA NPs into the spheroid structure. However, the quantitative analysis (Figure 8B) showed a higher internalization extent of CM−SRF−PDA NPs (8.2 ± 1.3%, in terms of fluorescence signal overlap between cells and nanoparticles) with respect to SRF−PDA NPs (5.3 ± 1.0%), suggesting a relevant contribution of the homotypic strategy even in 3D conditions.

Following the treatment with SRF, CM−PDA NPs, or CM−SRF−PDA NPs (with and without NIR stimulation and considering the respective controls), the shape and size of spheroids have been qualitatively analyzed with bright-field microscopy, and representative images are reported in Figure 8C. Major evident changes occurred after treatment with CM−SRF−PDA NPs, in particular in concomitance with NIR irradiation.

The therapeutic efficiency following NIR stimulation in SRF-, CM−PDA NP-, and CM−SRF−PDA NP-treated spheroids has again been quantitatively evaluated in terms of necrotic/apoptotic phenomena, as reported in Figure 8D (representative data in Figure S6A of the Supporting Information). SRF + NIR induced apoptosis and late apoptosis in 5.3 ± 1.6 and 16.2 ± 3.1% of cells, suggesting a significant effect even in 3D cultures. Also, the CM−PDA NPs + NIR and CM−SRF−PDA NPs + NIR treatments provided significant results, in terms of both necrosis (5.2 ± 1.7 and 5.6 ± 0.5%, in the two experimental classes, respectively) and late apoptosis (23.3 ± 8.5 and 22.1 ± 3.9%, in the two experimental classes, respectively), suggesting a good outcome of the hyperthermia treatment also in 3D cultures.

3.6. *Ex Ovo* Validation. Still, in perspective of bringing the proposed nanoplatform closer to the pre-clinical testing, a final validation has been performed *ex ovo* on quail embryos (Figure 9). Quail embryos are relatively easy to obtain and maintain at a low cost with respect to murine models, and at the same time, they do not present substantial ethical issues if experiments are performed within 16 days after fertilization.[65] Grafting tumor cells onto quail embryos allows for the study of tumor heterogeneity within a developing organism and also monitoring of the tumor interaction with the host organism during its development. Embryos undergo rapid development, allowing researchers to observe tumor growth and drug effects over a relatively short period; this indeed provides quicker results with respect to slower developing mammalian models.[66] Considering the transparency of the CAM structure of quail embryos, it is easy to monitor tumor growth, invasion, vascularization, and drug response in a non-invasive way; this transparency facilitates analysis through imaging techniques, such as microscopy and *in vivo* imaging, providing valuable insights into the dynamics of tumor development.[67]

With adherence to the stated ethical period, i.e., limiting the tests within ED 16, a schema of the experimental design is
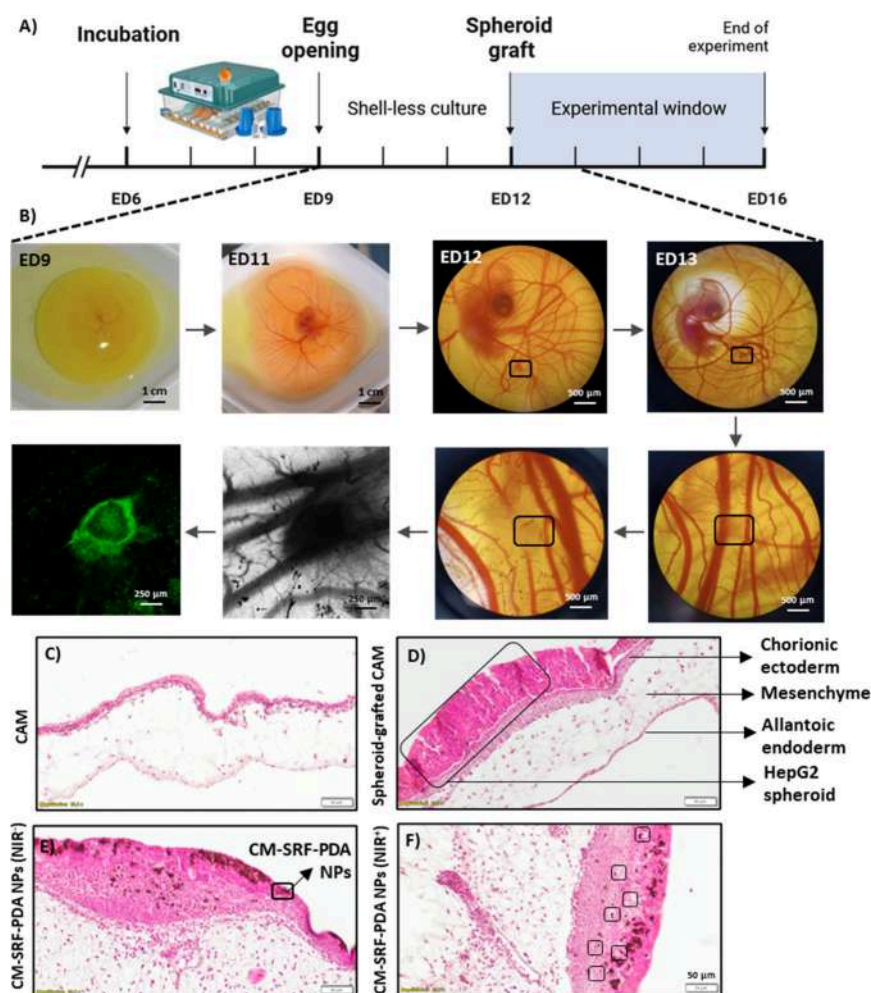
Figure 9. (A) Schematic representation of *ex ovo* experiments. (B) Representative bright-field microscopy images of the quail embryo CAM model at ED 9 and ED 11, HepG2 spheroid grafted in the CAM model (indicated with a black square) at ED 12, spheroid vascularization and CM−SRF−PDA NP injection ED 13, and confocal light transmission and fluorescence images showing nanoparticle (in green) internalization by the xenograft. Representative histological analysis images of (C) CAM, (D) HepG2 spheroid-grafted CAM, highlighted by the black square, (E) CM−SRF−PDA NP treatment, and (F) CM−SRF−PDA NP + NIR treatment. In panels E and F, black squares indicate nanoparticle clusters.

reported in Figure 9A. The quail embryos were left shell-less, placed in a Petri dish at ED 9, and incubated in optimal conditions until HepG2 cell spheroids were grafted in the CAM of embryos at ED 12, as indicated in Figure 9B. CM−SRF−PDA NPs were placed on top of the grafted tumor at ED 13, and after 24 h of incubation, the specimen was observed with the confocal microscope, highlighting a strong accumulation of the nanovectors in the grafted spheroid.

Following NIR treatment, histological analysis has been performed, by staining the nuclear compartment of the cells with hematoxylin (purple color) and collagen and elastin fibers with eosin (pink color). Figure 9C highlights the trilayered structure of the CAM, including the chorionic ectoderm, the fused mesenchymal layer, and the allantoic endoderm. In Figure 9D, the HCC xenograft is visible, located on the ectoderm layer of the CAM; however, cancer cell invasion through the ectoderm and spreading into the mesenchymal layer is appreciable, as also visible in the CM−SRF−PDA NP-treated sample (Figure 9E). In the same image, nanoparticles are visible, in particular throughout all of the spheroid structure. Following NIR stimulation, necrosis-dependent decellularized areas have been detected just around the CM−SRF−PDA NPs (black squares in Figure 9F) as well as discoloration of the nuclear components of

tumor cells in the rest of the spheroids. The necrotic areas around the nanostructures occur following NIR-mediated hyperthermia. Moreover, the discolored nuclei could be a potential hint of cellular apoptosis.

All of these outcomes are coherent with literature data describing the combined effects of chemotherapy and hyperthermia on different HCC models.[68] As an example, with regard to the effectiveness of photothermal ablation, the photothermal conversion capacity of polymeric pH-sensitive camptothecin (CPT)-tethered PDA NPs (PDA@PCPT NPs) has been evaluated *in vivo* using a tumor-bearing mouse model. Following the intravenous injection of PDA@PCPT NPs, a 10 min exposure to a 808 nm laser (2.0 W/cm^2) rapidly increased the temperature at the tumor tissues from 34.5 to 56 °C. Furthermore, the tumor inhibitory rate of PDA@PCPT combined with NIR irradiation achieved 92.8%, suggesting an excellent *in vivo* photothermal effect of PDA@PCPT NPs.[69] In another *in vivo* evaluation, Liu and colleagues assessed NIR-induced hyperthermia for the ablation of central nervous system cancers localized in deep brain tissue.[70] At 30 min after the injection, the rat brain was exposed to NIR laser irradiation (808 nm) for 10 min. The temperature increment in the laser-focused

zone exceeded 60 °C after 6 min of irradiation, leading to a precise and localized ablation of deep brain tissues.[70]

4. CONCLUSION

This study proposes the exploitation of polydopamine nanoparticles for combined chemotherapy and photothermal therapy, with a targeted focus on liver cancer, presenting a promising avenue for effective clinical treatments. The homotypic targeting strategy was successful, indicating a 2-fold higher uptake in cancer cells with respect to healthy cells; furthermore, the cell membrane coating provided a 3-fold higher internalization extent with respect to non-coated nanostructures. The efficacy of this multi-therapeutic strategy has been assessed through different models, including 2D cell cultures, 3D HepG2-derived spheroids, and an *ex ovo* model employing a HepG2 spheroid-grafted chorioallantoic membrane in quail eggs. Besides a significant cancer cell viability reduction, the combined treatment provided an increased stress response against hyperthermia and induction of apoptotic phenomena. A comprehensive evaluation has been eventually performed, integrating proteomic analysis to elucidate the molecular mechanisms underlying the therapeutic effects and identify potential biomarkers for monitoring the treatment response. In conclusion, the collected findings provide compelling evidence for a promising clinical translation of a PDA NP-mediated multifunctional treatment of liver cancer.

■ ASSOCIATED CONTENT

Data Availability Statement

Proteomics data are available via ProteomeXchange with identifier PXD051299.

Ⓢ Supporting Information

The Supporting Information is available free of charge at https://pubs.acs.org/doi/10.1021/acsami.4c08491.

> Schema of the microfluidic system, finite element modeling simulation of the flows inside the microfluidic system and experimental setup, concentration-dependent cell metabolic activity and viability evaluation, characterization of rhodamine-loaded nanoparticles, and data from representative flow cytometry experiments (PDF)

■ AUTHOR INFORMATION

Corresponding Authors

Gianni Ciofani − *Smart Bio-Interfaces, Istituto Italiano di Tecnologia, 56025 Pontedera, Italy;* ⒾD orcid.org/0000-0003-1192-3647; Email: gianni.ciofani@iit.it

Melis Emanet − *Smart Bio-Interfaces, Istituto Italiano di Tecnologia, 56025 Pontedera, Italy;* ⒾD orcid.org/0000-0001-9512-3844; Email: melis.emanetciofani@iit.it

Authors

Marie Celine Lefevre − *Smart Bio-Interfaces, Istituto Italiano di Tecnologia, 56025 Pontedera, Italy*

Maria Cristina Ceccarelli − *Smart Bio-Interfaces, Istituto Italiano di Tecnologia, 56025 Pontedera, Italy; The BioRobotics Institute, Scuola Superiore Sant'Anna, 56025 Pontedera, Italy*

Matteo Battaglini − *Smart Bio-Interfaces, Istituto Italiano di Tecnologia, 56025 Pontedera, Italy*

Alessio Carmignani − *Smart Bio-Interfaces, Istituto Italiano di Tecnologia, 56025 Pontedera, Italy;* ⒾD orcid.org/0000-0002-6316-3478

Francesco Schiavone − *Smart Bio-Interfaces, Istituto Italiano di Tecnologia, 56025 Pontedera, Italy*

Attilio Marino − *Smart Bio-Interfaces, Istituto Italiano di Tecnologia, 56025 Pontedera, Italy;* ⒾD orcid.org/0000-0002-3290-494X

Daniele De Pasquale − *Smart Bio-Interfaces, Istituto Italiano di Tecnologia, 56025 Pontedera, Italy;* ⒾD orcid.org/0000-0001-7219-2396

Mirko Prato − *Materials Characterization Facility, Istituto Italiano di Tecnologia, 16163 Genova, Italy;* ⒾD orcid.org/0000-0002-2188-8059

Francesco De Boni − *Materials Characterization Facility, Istituto Italiano di Tecnologia, 16163 Genova, Italy;* ⒾD orcid.org/0000-0001-5285-1008

Andrea Petretto − *Core Facilities—Clinical Proteomics and Metabolomics, IRCCS Istituto Giannina Gaslini, 16147 Genova, Italy;* ⒾD orcid.org/0000-0001-7811-8517

Martina Bartolucci − *Core Facilities—Clinical Proteomics and Metabolomics, IRCCS Istituto Giannina Gaslini, 16147 Genova, Italy;* ⒾD orcid.org/0000-0001-5289-4219

Federico Catalano − *Electron Microscopy Facility, Istituto Italiano di Tecnologia, 16163 Genova, Italy;* ⒾD orcid.org/0000-0001-5574-0063

Stefania Moscato − *Department of Clinical and Experimental Medicine, University of Pisa, 56126 Pisa, Italy;* ⒾD orcid.org/0000-0001-9283-6902

Complete contact information is available at:
https://pubs.acs.org/10.1021/acsami.4c08491

Author Contributions

Melis Emanet, investigation, methodology, validation, conceptualization, data curation, formal analysis, and writing—original draft; Marie Celine Lefevre, investigation, methodology, data curation, formal analysis, and writing—original draft; Maria Cristina Ceccarelli, investigation, methodology, and writing—original draft; Matteo Battaglini, investigation, methodology, and data curation; Alessio Carmignani, investigation, methodology, and data curation; Francesco Schiavone, investigation, methodology, and data curation; Attilio Marino, data curation, formal analysis, investigation, and methodology; Daniele De Pasquale, investigation and methodology; Mirko Prato, resources, methodology, data curation, and formal analysis; Francesco De Boni, methodology, data curation, and formal analysis; Andrea Petretto, resources, methodology, data curation, and formal analysis; Martina Bartolucci, methodology, data curation, and formal Analysis; Federico Catalano, methodology, data curation, and formal analysis; Stefania Moscato, resources, methodology, validation, data curation, and formal analysis; and Gianni Ciofani, conceptualization, resources, supervision, project administration, and writing—review and editing.

Notes

The authors declare no competing financial interest.

■ REFERENCES

(1) Fattovich, G.; Stroffolini, T.; Zagni, I.; Donato, F. Hepatocellular carcinoma in cirrhosis: Incidence and risk factors. *Gastroenterology* **2004**, *127* (5), S35−S50.

(2) Mazzaferro, V.; Regalia, E.; Doci, R.; Andreola, S.; Pulvirenti, A.; Bozzetti, F.; Montalto, F.; Ammatuna, M.; Morabito, A.; Gennari, L. Liver transplantation for the treatment of small hepatocellular carcinomas in patients with cirrhosis. *N. Engl. J. Med.* **1996**, *334* (11), 693−699.

(3) Llovet, J. M.; Di Bisceglie, A. M.; Bruix, J.; Kramer, B. S.; Lencioni, R.; Zhu, A. X.; Sherman, M.; Schwartz, M.; Lotze, M.; Talwalkar, J.; Gores, G. J. Design and endpoints of clinical trials in hepatocellular carcinoma, J. *Natl. Res. Inst.* **2008**, *100* (10), 698−711.

(4) Nowak, A. K.; Chow, P. K. H.; Findlay, M. Systemic therapy for advanced hepatocellular carcinoma: A review. *Eur. J. Cancer.* **2004**, *40* (10), 1474−1484.

(5) Sacco, R.; Bargellini, I.; Gianluigi, G.; Bertini, M.; Bozzi, E.; Altomare, E.; Battaglia, V.; Romano, A.; Bertoni, M.; Capria, A.; Bresci, G.; Bartolozzi, C. Complete response for advanced liver cancer during sorafenib therapy: Case report. *BMC Gastroenterol.* **2011**, *11*, 4.

(6) Keating, G. M.; Santoro, A. Sorafenib: A review of its use in advanced hepatocellular carcinoma. *Drugs* **2009**, *69* (2), 223−240.

(7) El-Sheikh, S. M.; Khairy, M. H.; Osama, E.; Metwally, M. M.; Galal, A. A. Nanotechnology improves the therapeutic efficacy of gemcitabine against a human hepatocellular carcinoma cell line and minimizes its in vivo side effects. *Naunyn-Schmiedeberg's Arch. Pharmacol.* **2021**, *394*, 631−643.

(8) Pierini, F.; Nakielski, P.; Urbanek, O.; Pawłowska, S.; Lanzi, M.; De Sio, L.; Kowalewski, T. A. Polymer-based nanomaterials for photothermal therapy: From light-responsive to multifunctional nanoplatforms for synergistically combined technologies. *Biomacromolecules* **2018**, *19* (11), 4147−4167.

(9) Tahir, N.; Madni, A.; Li, W.; Correia, A.; Khan, M. M.; Rahim, M. A.; Santos, H. A. Microfluidic fabrication and characterization of Sorafenib-loaded lipid-polymer hybrid nanoparticles for controlled drug delivery. *Int. J. Pharm.* **2020**, *581*, 119275.

(10) Chen, J.; Sheu, A. Y.; Li, W.; Zhang, Z.; Kim, D. H.; Lewandowski, R. J.; Omary, R. A.; Shea, L. D.; Larson, A. C. Poly(lactide-co-glycolide) microspheres for MRI-monitored transcatheter delivery of sorafenib to liver tumors. *J. Control Release* **2014**, *184*, 10−17.

(11) Iacobazzi, R. M.; Vischio, F.; Arduino, I.; Canepa, F.; Laquintana, V.; Notarnicola, M.; Scavo, M. P.; Bianco, G.; Fanizza, E.; Lopedota, A. A.; Cutrignelli, A.; Lopalco, A.; Azzariti, A.; Curri, M. L.; Franco, M.; Giannelli, G.; Lee, B. C.; Depalo, N.; Denora, N. Magnetic implants in vivo guiding sorafenib liver delivery by superparamagnetic solid lipid nanoparticles. *J. Colloid Interface Sci.* **2022**, *608*, 239−254.

(12) Tran, H. T.; Vong, L. B.; Nishikawa, Y.; Nagasaki, Y. Sorafenib-loaded silica-containing redox nanoparticles for oral anti-liver fibrosis therapy. *J. Controlled Release* **2022**, *345*, 880−891.

(13) Yang, W.; Xia, B.; Wang, L.; Ma, S.; Liang, H.; Wang, D.; Huang, J. Shape effects of gold nanoparticles in photothermal cancer therapy. *Mater. Today Sustainability* **2021**, *13*, 100078.

(14) Giner-Casares, J. J.; Henriksen-Lacey, M.; Coronado-Puchau, M.; Liz-Marzán, L. M. Inorganic nanoparticles for biomedicine: Where materials scientists meet medical research. *Mater. Today* **2016**, *19* (1), 19−28.

(15) Battaglini, M.; Emanet, M.; Carmignani, A.; Ciofani, G. Polydopamine-based nanostructures: A new generation of versatile, multi-tasking, and smart theranostic tools. *Nano Today* **2024**, *55*, 102151.

(16) Chen, H. Y.; Deng, J.; Wang, Y.; Wu, C. Q.; Li, X.; Dai, H. W. Hybrid cell membrane-coated nanoparticles: A multifunctional biomimetic platform for cancer diagnosis and therapy. *Acta Biomater.* **2020**, *112*, 1−13.

(17) Harris, J. C.; Scully, M. A.; Day, E. S. Cancer cell membrane-coated nanoparticles for cancer management. *Cancers* **2019**, *11* (12), 1836.

(18) De Pasquale, D.; Pucci, C.; Desii, A.; Marino, A.; Debellis, D.; Leoncino, L.; Prato, M.; Moscato, S.; Amadio, S.; Fiaschi, P.; Prior, A.; Ciofani, G. A novel patient-personalized nanovector based on homotypic recognition and magnetic hyperthermia for an efficient treatment of glioblastoma multiforme. *Adv. Healthcare Mater.* **2023**, *12* (19), 2203120.

(19) Carmignani, A.; Battaglini, M.; Sinibaldi, E.; Marino, A.; Vighetto, V.; Cauda, V.; Ciofani, G. In vitro and ex vivo investigation of the effects of polydopamine nanoparticle size on their antioxidant and photothermal properties: Implications for biomedical applications. *ACS Appl. Nano Mater.* **2022**, *5*, 1702−1713.

(20) De Pasquale, D.; Marino, A.; Tapeinos, C.; Pucci, C.; Rocchiccioli, S.; Michelucci, E.; Finamore, F.; McDonnell, L.; Scarpellini, A.; Lauciello, S.; Prato, M.; Larrañaga, A.; Drago, F.; Ciofani, G. Homotypic targeting and drug delivery in glioblastoma cells through cell membrane-coated boron nitride nanotubes. *Mater. Des.* **2020**, *192*, 108742.

(21) Poon, C. Measuring the density and viscosity of culture media for optimized computational fluid dynamics analysis of in vitro devices, J. *Mech. Behav. Biomed. Mater.* **2022**, *126*, 105024.

(22) Lee, S. Y.; Kim, D.; Lee, S. H.; Sung, J. H. Microtechnology-based in vitro models: Mimicking liver function and pathophysiology. *APL Bioeng.* **2021**, *5* (4), 041505.

(23) Marino, A.; Camponovo, A.; Degl'Innocenti, A.; Bartolucci, M.; Tapeinos, C.; Martinelli, C.; De Pasquale, D.; Santoro, F.; Mollo, V.; Arai, S.; Suzuki, M.; Harada, Y.; Petretto, A.; Ciofani, G. Multifunctional temozolomide-loaded lipid superparamagnetic nanovectors: Dual targeting and disintegration of glioblastoma spheroids by synergic chemotherapy and hyperthermia treatment. *Nanoscale* **2019**, *11* (44), 21227−21248.

(24) Bruderer, R.; Bernhardt, O. M.; Gandhi, T.; Miladinović, S. M.; Cheng, L. Y.; Messner, S.; Ehrenberger, S. T.; Zanotelli, V.; Butscheid, Y.; Escher, C.; Vitek, O.; Rinner, O.; Reiter, L. Extending the limits of quantitative proteome profiling with data-independent acquisition and application to acetaminophen-treated three-dimensional liver microtissues. *Mol. Cell. Proteomics* **2015**, *14* (5), 1400−1410.

(25) Tyanova, S.; Temu, T.; Sinitcyn, P.; Carlson, A.; Hein, M. Y.; Geiger, T.; Mann, M.; Cox, J. The Perseus Computational Platform for Comprehensive Analysis of (Prote) Omics Data. *Nat. Methods* **2016**, *13* (9), 731−740.

(26) Greene, C. S.; Krishnan, A.; Wong, A. K.; Ricciotti, E.; Zelaya, R. A.; Himmelstein, D. S.; Zhang, R.; Hartmann, B. M.; Zaslavsky, E.; Sealfon, S. C.; Chasman, D. I.; FitzGerald, G. A.; Dolinski, K.; Grosser, T.; Troyanskaya, O. G. Understanding multicellular function and disease with human tissue-specific networks. *Nat. Genet.* **2015**, *47* (6), 569−576.

(27) Mallinson, D.; Mullen, A. B.; Lamprou, D. A. Probing polydopamine adhesion to protein and polymer films: Microscopic and spectroscopic evaluation. *J. Mater. Sci.* **2018**, *53* (5), 3198−3209.

(28) Shimizu, K.; Takeoka, S. Photothermal switch of drug release from polydopamine-modified nanosheets. *MRS Commun.* **2023**, *13* (5), 818−824.

(29) Lu, J.; Cai, L.; Dai, Y.; Liu, Y.; Zuo, F.; Ni, C.; Shi, M.; Li, J. Polydopamine-based nanoparticles for photothermal therapy/chemotherapy and their synergistic therapy with autophagy inhibitor to promote antitumor treatment. *Chem. Rec.* **2021**, *21* (4), 781−796.

(30) Ray, S.; Shard, A. G. Quantitative analysis of adsorbed proteins by X-ray photoelectron spectroscopy. *Anal. Chem.* **2011**, *83* (22), 8659−8666.

(31) Lee, H.; Rho, J.; Messersmith, P. B. Facile conjugation of biomolecules onto surfaces via mussel adhesive protein inspired coatings. *Adv. Mater.* **2009**, *21* (4), 431.

(32) Hemmatpour, H.; De Luca, O.; Crestani, D.; Stuart, M. C. A.; Lasorsa, A.; van der Wel, P. C. A.; Loos, K.; Giousis, T.; Haddadi-Asl, V.; Rudolf, P. New insights in polydopamine formation via surface adsorption. *Nat. Commun.* **2023**, *14*, 664.

(33) Rojas, J. V.; Toro-Gonzalez, M.; Molina-Higgins, M. C.; Castano, C. E. Facile radiolytic synthesis of ruthenium nanoparticles on graphene oxide and carbon nanotubes, *Mater. Sci. Eng. B* **2016**, *205*, 28−35.

(34) Peng, B.; Xu, Y.; Liu, K.; Wang, X.; Mulder, F. M. High-Performance and Low-Cost Sodium-Ion Anode Based on a Facile Black Phosphorus Carbon Nanocomposite. *ChemElectroChem* **2017**, *4*, 2140−2144.

(35) Sheng, X.; Huang, T.; Qin, J.; Li, Q.; Wang, W.; Deng, L.; Dong, A. Preparation, pharmacokinetics, tissue distribution and antitumor effect of sorafenib-incorporating nanoparticles in vivo. *Oncol. Lett.* **2017**, *14* (5), 6163−6169.

(36) Baracca, A.; Sgarbi, G.; Solaini, G.; Lenaz, G. Rhodamine 123 as a probe of mitochondrial membrane potential: Evaluation of proton flux through F0 during ATP synthesis. *Biochim. Biophys. Acta, Bioenerg.* **2003**, *1606*, 137−146.

(37) Pang, Y.; Eresen, A.; Zhang, Z.; Hou, Q.; Wang, Y.; Yaghmai, V.; Zhang, Z. Adverse events of sorafenib in hepatocellular carcinoma treatment. *Am. J. Cancer Res.* **2022**, *12* (6), 2770−2782.

(38) Gupta, A. K.; Gupta, M. Cytotoxicity suppression and cellular uptake enhancement of surface modified magnetic nanoparticles. *Biomaterials* **2005**, *26* (13), 1565−1573.

(39) Chen, B.; Feder, M. E.; Kang, L. Evolution of heat-shock protein expression underlying adaptive responses to environmental stress. *Mol. Ecol.* **2018**, *27* (15), 3040−3054.

(40) Zheng, Y.; Jia, R.; Li, J.; Tian, X.; Qian, Y. Curcumin-and resveratrol-co-loaded nanoparticles in synergistic treatment of hepatocellular carcinoma. *J. Nanobiotechnol.* **2022**, *20* (1), 339.

(41) El-Sewedy, T.; Salama, A. F.; Mohamed, A. E.; Elbaioumy, N. M.; El-Far, A. H.; Albalawi, A. N.; Elmetwalli, A. Hepatocellular carcinoma cells: Activity of amygdalin and sorafenib in targeting AMPK/mTOR and BCL-2 for anti-angiogenesis and apoptosis cell death. *BMC Complement. Med. Ther.* **2023**, *23* (1), 329.

(42) Liu, L.; Cao, Y.; Chen, C.; Zhang, X.; McNabola, A.; Wilkie, D.; Wilhelm, S.; Lynch, M.; Carter, C. Sorafenib blocks the RAF/MEK/ERK pathway, inhibits tumor angiogenesis, and induces tumor cell apoptosis in hepatocellular carcinoma model PLC/PRF/5. *Cancer Res.* **2006**, *66* (24), 11851−11858.

(43) Ebrahim, H. M.; El-Rouby, M. N.; Morsy, M. E.; Said, M. M.; Ezz, M. K. The synergistic cytotoxic effect of laser-irradiated gold nanoparticles and sorafenib against the growth of a human hepatocellular carcinoma cell line, Asian Pac. *J. Cancer Prev.* **2019**, *20*, 3369−3376.

(44) Garten, A.; Grohmann, T.; Kluckova, K.; Lavery, G. G.; Kiess, W.; Penke, M. Sorafenib-induced apoptosis in hepatocellular carcinoma is reversed by SIRT1. *Int. J. Mol. Sci.* **2019**, *20* (16), 4048.

(45) Liu, J.; Abshire, C.; Carry, C.; Sholl, A. B.; Mandava, S. H.; Datta, A.; Ranjan, M.; Callaghan, C.; Peralta, D. V.; Williams, K. S.; Lai, W. R.; Abdel-Mageed, A. B.; Tarr, M.; Lee, B. R. Nanotechnology combined therapy: Tyrosine kinase-bound gold nanorod and laser thermal ablation produce a synergistic higher treatment response of renal cell carcinoma in a murine model. *BJU Int.* **2017**, *119*, 342−348.

(46) Zheng, J.; Zeng, L.; Tang, M.; Lin, H.; Pi, C.; Xu, R.; Cui, R. X. Novel Ferrocene Derivatives Induce G0/G1 Cell Cycle Arrest and Apoptosis through the Mitochondrial Pathway in Human Hepatocellular Carcinoma. *Int. J. Mol. Sci.* **2021**, *22* (6), 3097.

(47) Nguyen, L. M. D.; Malamo, A. G.; Larkin-Kaiser, K. A.; Borsa, P. A.; Adhihetty, P. J. Effect of near-infrared light exposure on mitochondrial signaling in C2C12 muscle cells. *Mitochondrion* **2014**, *14*, 42−48.

(48) Oei, A. L.; Vriend, L. E. M.; Crezee, J.; Franken, N. A. P.; Krawczyk, P. M. Effects of hyperthermia on DNA repair pathways: One treatment to inhibit them all. *Radiat Oncol.* **2015**, *10*, 165−178.

(49) Linke, S. P.; Clarkin, K. C.; Di Leonardo, A.; Tsou, A.; Wahl, G. M. A reversible, p53-dependent G0/G1 cell cycle arrest induced by ribonucleotide depletion in the absence of detectable DNA damage. *Genes Dev.* **1996**, *10*, 934−947.

(50) Shen, H.; Wang, L.; Zhang, J.; Dong, W.; Zhang, T.; Ni, Y.; Cao, H.; Wang, K.; Li, Y.; Wang, Y.; Du, J. ARRB1 enhances the chemosensitivity of lung cancer through the mediation of DNA damage response. *Oncology reports* **2017**, *37* (2), 761−767.

(51) Shen, J.-D.; Fu, S.-Z.; Ju, L.-L.; Wang, Y.-F.; Dai, F.; Liu, Z.-X.; Ji, H.-Z.; Shao, J.-G.; Bian, Z.-L. High expression of ubiquitin-conjugating enzyme E2A predicts poor prognosis in hepatocellular carcinoma. *Oncol. Lett.* **2018**, *15* (5), 7362−7368.

(52) Mosser, D. D.; Caron, A. W.; Bourget, L.; Denis-Larose, C.; Massie, B. Role of the human heat shock protein hsp70 in protection against stress-induced apoptosis. *Mol. Cell. Biol.* **1997**, *17* (9), 5317−5327.

(53) Stankiewicz, A. R.; Lachapelle, G.; Foo, C. P.; Radicioni, S. M.; Mosser, D. D. Hsp70 inhibits heat-induced apoptosis upstream of mitochondria by preventing Bax translocation. *J. Biol. Chem.* **2005**, *280* (46), 38729−38739.

(54) Lin, B.; Zhou, X.; Lin, S.; Wang, X.; Zhang, M.; Cao, B.; Dong, Y.; Yang, S.; Wang, J. M.; Guo, M.; Huang, J. Epigenetic silencing of PRSS3 provides growth and metastasis advantage for human hepatocellular carcinoma. *J. Mol. Med.* **2017**, *95*, 1237−1249.

(55) Eells, J. T.; Wong-Riley, M. T. T.; VerHoeve, J.; Henry, M.; Buchman, E. V.; Kane, M. P.; Gould, L. J.; Das, R.; Jett, M.; Hodgson, B. D. Mitochondrial signal transduction in accelerated wound and retinal healing by near-infrared light therapy. *Mitochondrion* **2004**, *4* (5−6), 559−567.

(56) Jacobs, D. T.; Weigert, R.; Grode, K. D.; Donaldson, J. G.; Cheney, R. E. Myosin Vc is a molecular motor that functions in secretory granule trafficking, Mol. *Biol. Cell.* **2009**, *20* (21), 4471−4488.

(57) Spillare, E. A.; Wang, X. W.; Von Kobbe, C.; Bohr, V. A.; Hickson, I. D.; Harris, C. C. Redundancy of DNA helicases in p53-mediated apoptosis. *Oncogene* **2006**, *25* (14), 2119−2123.

(58) Tang, W.; Lv, B.; Yang, B.; Chen, Y.; Yuan, F.; Ma, L.; Chen, S.; Zhang, S.; Xia, J. TREM2 acts as a tumor suppressor in hepatocellular carcinoma by targeting the PI3K/Akt/β-catenin pathway. *Oncogenesis* **2019**, *8* (2), 9.

(59) Liu, X.; Ou, H.; Xiang, L.; Li, X.; Huang, Y.; Yang, D. Elevated UHRF1 expression contributes to poor prognosis by promoting cell proliferation and metastasis in hepatocellular carcinoma. *Oncotarget* **2017**, *8* (6), 10510.

(60) Wu, S.-Y.; Chiang, C.-M. TATA-binding protein-associated factors enhance the recruitment of RNA polymerase II by transcriptional activators. *J. Biol. Chem.* **2001**, *276* (36), 34235−34243.

(61) Hampsey, M.; Reinberg, D. Transcription: Why are TAFs essential? *Curr. Biol.* **1997**, *7* (1), R44−R46.

(62) Freie, B.; Li, X.; Ciccone, S. L.; Nawa, K.; Cooper, S.; Vogelweid, C.; Schantz, L.; Haneline, L. S.; Orazi, A.; Broxmeyer, H. E.; Lee, S. H.; Clapp, D. W. Fanconi anemia type C and p53 cooperate in apoptosis and tumorigenesis. *Blood* **2003**, *102* (12), 4146−4152.

(63) Xia, L.; Huang, W.; Bellani, M.; Seidman, M. M.; Wu, K.; Fan, D.; Nie, Y.; Cai, Y.; Zhang, Y. W.; Yu, L.-R.; Li, H.; Zahnow, C. A.; Xie, W.; Chiu Yen, R.-W.; Rassool, F. V.; Baylin, S. B. CHD4 has oncogenic functions in initiating and maintaining epigenetic suppression of multiple tumor suppressor genes. *Cancer Cell* **2017**, *31* (5), 653−668.e7.

(64) Repenning, A.; Happel, D.; Bouchard, C.; Meixner, M.; Verel-Yilmaz, Y.; Raifer, H.; Holembowski, L.; Krause, E.; Kremmer, E.; Feederle, R.; Keber, C. U; Lohoff, M.; Slater, E. P; Bartsch, D. K; Bauer, U.-M. PRMT1 promotes the tumor suppressor function of p14ARF and is indicative for pancreatic cancer prognosis. *EMBO J.* **2021**, *40* (13), No. e106777.

(65) Kundeková, B.; Máčajová, M.; Meta, M.; Čavarga, I.; Bilčík, B. Chorioallantoic membrane models of various avian species: Differences and applications. *Biology* **2021**, *10* (4), 301.

(66) Hall, J.; Jheon, A. H.; Ealba, E. L.; Eames, B. F.; Butcher, K. D.; Mak, S.-S.; Ladher, R.; Alliston, T.; Schneider, R. A. Evolution of a developmental mechanism: Species-specific regulation of the cell cycle and the timing of events during craniofacial osteogenesis. *Dev. Biol.* **2014**, *385* (2), 380−395.

(67) Huss, D.; Benazeraf, B.; Wallingford, A.; Filla, M.; Yang, J.; Fraser, S. E.; Lansford, R. A transgenic quail model that enables dynamic imaging of amniote embryogenesis. *Development* **2015**, *142* (16), 2850−2859.

(68) Medina-Ramírez, I. E.; Díaz de León Olmos, M. A.; Munoz Ortega, M. H.; Zapien, J. A.; Betancourt, I.; Santoyo-Elvira, N. Development and assessment of nano-technologies for cancer treat-

ment: Cytotoxicity and hyperthermia laboratory studies. *Cancer Invest.* **2020**, *38* (1), 61−84.

(69) Zhang, H.; Sun, Y.; Huang, R.; Cang, H.; Cai, Z.; Sun, B. pH-sensitive prodrug conjugated polydopamine for NIR-triggered synergistic chemo-photothermal therapy. *Eur. J. Pharm. Biopharm.* **2018**, *128*, 260−271.

(70) Liu, J. S.; Peng, S. J.; Li, G. F.; Zhao, Y. X.; Meng, X. Y.; Yu, X. R.; Li, Z. H.; Chen, J. M. Polydopamine nanoparticles for deep brain ablation via near-infrared irradiation. *ACS Biomater. Sci. Eng.* **2020**, *6* (1), 664−672.